FACULTY
OF MATHEMATICS
AND PHYSICS
Charles University

BACHELOR THESIS

Antonín Baďura

Thermo-transport effects in antiferromagnets

Department of Chemical Physics and Optics

Supervisor of the bachelor thesis:	RNDr. Eva Schmoranzerová, Ph.D.
Study programme:	Physics
Study branch:	General Physics

Prague 2020

I declare that I carried out this bachelor thesis independently, and only with the cited sources, literature and other professional sources. It has not been used to obtain another or the same degree.

I understand that my work relates to the rights and obligations under the Act No. 121/2000 Sb., the Copyright Act, as amended, in particular the fact that the Charles University has the right to conclude a license agreement on the use of this work as a school work pursuant to Section 60 subsection 1 of the Copyright Act.

In .... date ....

Author's signature

Acknowledgements

In the first place, I would like to express my gratitude to Prof. Petr Němec, who has, very kindly, prepared and offered me several topics for this thesis.

I also want to thank Lisa Michez from the Centre Interdisciplinaire de Nanoscience de Marseille for growing the samples and to Rafael Lopes Seeger who prepared most of the lithography structures and have substantially participated on the magnetotransport measurements in Dresden. I am also profoundly grateful to members of the group of Prof. Sebastian T. B. Goennenwein at the Technical University Dresden where the magnetotransport and thermotransport experiments were performed. Especially I would like to thank Helena Reichlová for enabling me to participate in her project and for a valuable discussion of the results, and also Richard Schlitz for his guidance and assistance during the magnetotransport measurements and the data analysis.

I am also very grateful to my consultant Tomáš Ostatnický for his guidance through the process of mathematical modelling.

Yet none of the aforementioned would be possible without careful and supportive guidance of Eva Schmoranzerová, whom I owe my deepest gratitude.

Title Thermo-transport effects in antiferromagnets

Author Antonín Baďura

Department Department of Chemical Physics and Optics

Supervisor RNDr. Eva Schmoranzerová, Ph.D., Department of Chemical Physics and Optics

Abstract This thesis investigates magnetic properties of an antiferromagnet Mn_5Si_3 in both collinear and noncollinear antiferromagnetic phases, which this compound evinces. The work is based on three distinct experimental approaches: The first one comprises measurements of magnetotransport phenomena (namely anisotropic magnetoresistance and Hall effects), the second one studies thermal counterparts of these effects (particularly the anomalous Nernst effect). Finally, we used scanning thermal gradient microscopy in order to observe the domain structure of Mn_5Si_3. The key outcome of the magnetotransport measurements is an observation of the Hall response in the collinear antiferromagnetic phase, which we attribute to the recently proposed crystal Hall effect. Furthermore, the thermotransport measurements resulted in the first observation of the anomalous Nernst effect in this compound. Due to the variety of artefacts, we did not record any convincing image of the domain structure in Mn_5Si_3. The analysis of the artefacts was supported by mathematical modelling that helped to pinpoint their origin.

Keywords antiferromagnetism, Hall effect, Nernst effect, magnetoresistance, domain structure.

Contents

Introduction **3**

1 Theoretical background **5**
- 1.1 Magnetism and magnetic order 5
- 1.2 Magnetotransport phenomena in antiferromagnets 8
  - 1.2.1 Magnetoresistance 8
  - 1.2.2 Hall effects 9
- 1.3 Thermotransport effects in antiferromagnets 10
  - 1.3.1 Seebeck effect 10
  - 1.3.2 Magnetoresistance 11
  - 1.3.3 Nernst effects 11

2 Experimental methods and materials **13**
- 2.1 Materials and samples 13
  - 2.1.1 Mn_5Si_3 13
  - 2.1.2 Samples 14
  - 2.1.3 Magnetic characterization 15
  - 2.1.4 Devices 15
- 2.2 Experimental methods 16
  - 2.2.1 Magnetotransport measurements 16
  - 2.2.2 Thermotransport measurements 18
  - 2.2.3 Scanning thermal gradient microscopy 21

3 Experimental results **24**
- 3.1 Magnetotransport measurements 26
  - 3.1.1 Field sweeps 26
  - 3.1.2 Field rotations 34
- 3.2 Thermotransport measurements 35
- 3.3 Thermal gradient microscopy 38

4 Mathematical modelling **43**
- 4.1 Nernst artefacts 43
- 4.2 Seebeck artefacts in STGM 47

Conclusion **51**

Bibliography **53**

List of Figures **56**

List of Tables **57**

List of Abbreviations **58**

A Determination of laser spot width **59**

Introduction

Antiferromagnetism, the second type of magnetic ordering after ferromagnetism, was discovered in the 1930s and has been studied thoroughly ever since [1]. Yet even forty years later has not Louis Néel foreseen any possibility of their technological application, as he expressed in his Nobel lecture [2]: ”A large number of antiferromagnetic materials is now known: these are generally compounds of the transition metals containing oxygen or sulphur. They are extremely interesting from the theoretical viewpoint, but do not seem to have any applications.” After another four decades, antiferromagnets appear to play a significant role in many areas of microelectronics research [1].

The first technological application took place in the 1990s when an antiferromagnetic material was employed within a magnetic memory based on the giant magnetoresistance effect [3]. The latest developments in the field of antiferromagnetic spintronics are particularly profound [1]. Spintronics is a branch of condensed matter physics that includes a new degree of freedom, electron spin, to information storage which today relies mostly on the charge of electrons. Spintronic devices have been traditionally based on ferromagnetic materials [1]; however, antiferromagnets overcome particular issues and limitations connected to ferromagnetic order [3]. The major advantage of antiferromagnets is the absence of a stray field that limits downscaling of the memory cells. They are also expected to be faster (e.g. the writing speed in ferromagnets is limited by the GHz scale, compared to the physical limit of the THz scale for antiferromagnets) and less energy-consuming [1, 3].

Research in antiferromagnetic spintronics has so far focused mostly on its fundamental physics aspects such as the way of manipulating antiferromagnetic moments and the behaviour of magnetic structures [1]. In this thesis, we follow the same research direction in studying elementary magnetic properties of one particular antiferromagnetic compound Mn_5Si_3. This material shows exceptional temperature-dependent magnetic ordering that allows us to reach the collinear and the noncollinear antiferromagnetic state only by a change of temperature. Such property provides us with a unique opportunity to study magneto- and thermotransport phenomena (Hall effects and their thermal counterparts) of completely different origin within one sample. Results of this study may give us a valuable insight into the magnetic and crystal structure of Mn_5Si_3.

We shall examine the Mn_5Si_3 compound from three distinct perspectives. The first one should reflect its magnetic structure through the magnetotransport phenomena (such as magnetoresistance and Hall effects); secondly, we will measure the response of Mn_5Si_3 to thermotransport effects, and finally, we shall attempt to visualize its domain structure using scanning thermal gradient microscopy.

This thesis consists of four chapters. Firstly, we introduce fundamental concepts of magnetic ordering and related magnetic phenomena. The second one summarizes our knowledge of Mn_5Si_3 and describes samples and experimental methods in detail. In the following chapter, we report the results of our measurements. The last chapter describes our attempt to optimize the measurement and interpret our experimental results using mathematical modelling.

Chapter 1

Theoretical background

Throughout this work, we will deal with magnetism and mostly with a particular form of magnetic order, with antiferromagnetism. In the following pages, we are going to introduce fundamental concepts related to magnetism and magnetic ordering; nevertheless, more detailed description can be found in appropriate publications [4, 5]. Furthermore, we present a detailed overview of phenomena connected with the transport behaviour of magnetically ordered materials, which will play an essential role in our experiments.

1.1 Magnetism and magnetic order

The fundamental object in magnetism is the magnetic moment. Although classical electromagnetism failed to explain basic concepts of magnetism such as the ferromagnetic or paramagnetic order, the classical concept of the magnetic moment as a current loop can be at least considered as a useful approximation of reality. In this classical way, we define an infinitesimal magnetic moment $\mathrm{d}\boldsymbol{m}$ as

$$\mathrm{d}\boldsymbol{m} = I\mathrm{d}\boldsymbol{S}, \tag{1.1}$$

where I is the current flowing in the infinitesimal loop of an oriented area $\mathrm{d}\boldsymbol{S}$ [4].

A magnetic solid consists of a large number of atoms with magnetic moments. We, therefore, define a new quantity for the description of its magnetic state — magnetization $\boldsymbol{M}$ — as the total magnetic moment per unit volume. If we apply a magnetic field of intensity $\boldsymbol{H}$ to such a solid that is isotropic and homogeneous, we get a linear relationship between magnetization and the H-field:

$$\boldsymbol{M} = \chi\boldsymbol{H}. \tag{1.2}$$

Based on the constant of proportionality χ, susceptibility, we can divide macroscopic systems into several classes. The most usual division is summarized in Tab. 1.1. There are, however, also other magnetic configurations not mentioned in this table, such as ferrimagnetic or antiferromagnetic one. These magnetic structures are ordered similarly to ferromagnets, and also their susceptibility corresponds to the ferromagnetic class [3, 4].

In the following, we will describe in more detail some of the above-mentioned magnetic phases, which are relevant for our work. These are paramagnetic, ferromagnetic, and, most importantly, antiferromagnetic phases.

class	χ	examples
diamagnet	< 0	silicon, gold
paramagnet	10^{-3}–10^{-5}	aluminium, platinum
ferromagnet	$50 <$	iron, cobalt

Table 1.1: Classes of materials based on their susceptibility [3]. The table mentions three basic classes of materials, their typical values of susceptibility, and examples of such materials.

Paramagnetism As already mentioned, the paramagnetic state corresponds to the positive value of susceptibility or, in other words, an applied magnetic field induces magnetization in a paramagnet which aligns parallel to the field. When no magnetic field is present, magnetization of a paramagnet is zero, although individual paramagnetic atoms still have a nonzero magnetic moment due to the presence of unpaired electrons. (Unlike for diamagnets, where the atoms themself do not have any magnetic moment.) Because of a weak interaction among these moments, they point in random directions, which results in zero magnetization [4].

From the experimental point of view, there is a substantive relationship between the susceptibility of a paramagnet and temperature T, Curie's law:

$$\chi = \frac{C}{T}, \tag{1.3}$$

where C is a material constant. In the situation when a magnetically ordered material undergoes a transition to a paramagnetic state, the relation (1.3) transforms into a more general form, into the Curie-Weiss law:

$$\chi = \frac{C}{T - \theta}, \tag{1.4}$$

where the quantity θ is equal to the Curie temperature T_C for the transition ferromagnet-paramagnet and to the negative Néel temperature T_N for the transition antiferromagnet-paramagnet [3, 4].

Ferromagnetism In analogy to the paramagnetic phase, an atom in a ferromagnet also maintains a nonzero magnetic moment due to unpaired electrons. In this case, however, the interaction between the neighbouring moments is substantially stroger, which results in long-range magnetic order, where all the magnetic moments lie along a single unique direction (within one domain). As a consequence, a ferromagnet has a spontaneous magnetization even in the absence of an external magnetic field [3, 4].

Antiferromagnetism Individual atoms that comprise a crystal lattice of an antiferromagnet (AFM) also sustain nonzero magnetic moments as the ferromagnetic phase does. However, the negative exchange interaction leads to such magnetic order which prefers to keep two neighbouring moments perfectly antiparallel. As a result, net magnetization of an antiferromagnet is zero.

Magnetic order subdivides a crystal lattice of an antiferromagnet into two or more sublattices in which the magnetic moments are oriented in the same direction. Unlike in ferromagnets, spins are not necessarily oriented parallel (or antiparallel to be precise) but can even form a configuration where the moments do not lie in one plane. According to the configuration of spins, we can distinguish two basic types of the spin structure in an AFM: Firstly, there are *collinear* antiferromagnets with a defined axis (axes) along which all the spins are aligned. The condition of zero magnetization is then satisfied by coupling individual moments with opposite orientation. The second type is *noncollinear*, frustrated, antiferromagnetism, where the spins are not oriented antiparallel to each other, their coupling is substantially weaker, and can form complex noncollinear spin structures in order to reach zero net magnetization [3, 5]. Examples of both types are introduced in Fig. 1.1: Fig. 1.1 (a) shows the magnetic structure of collinear MnO, whereas Fig. 1.1 (b) presents the structure of a noncollinear AFM Mn_3Ir [3].

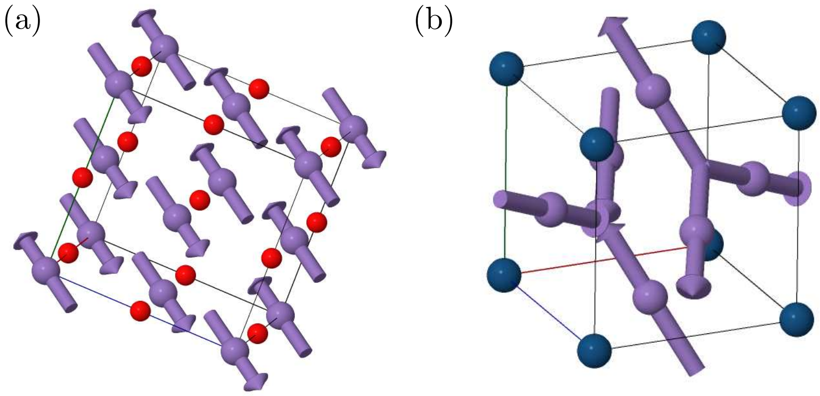

Figure 1.1: Examples of collinear and noncollinear antiferromagnets. The figure shows magnetic structure of (a) a collinear antiferromagnet MnO, (b) a noncollinear AFM Mn_3Ir [6].

Although the concept of magnetization lacks purpose for AFMs, a new quantity, the Néel vector $\boldsymbol{L}$, can be introduced in order to describe the direction of the moments in an antiferromagnet. In the case of collinear AFMs, $\boldsymbol{L}$ corresponds to the direction of individual spins [3]. In a noncollinear spin configuration, the spin chirality $\kappa = \sum \boldsymbol{S}_i \cdot (\boldsymbol{S}_k \times \boldsymbol{S}_l)$ of three magnetic moments spanning a triangle can induce a finite Berry phase and an associated fictitious magnetic field represented by a ghost vector $\boldsymbol{g}$ [7].

For the sake of simplicity, let us now consider only collinear AFMs. If we place such antiferromagnet into a strong magnetic field that is perpendicular to the Néel vector, spins in both sublattices bend in the direction of the field. By increasing its intensity, we can force the spins to line up with the magnetic field entirely. It can be shown that the susceptibility in this process is temperature-independent. In contrast, when the field is parallel to the antiferromagnetic axis, the spins do not exhibit any change in their direction; however, at a critical field, the moments suddenly switch to a position symmetrical around the AFM axis. In this process (called *spin-flip*), the susceptibility is an increasing function of temperature and reaches its maximum at the Néel temperature [4, 5].

If we combine the aforementioned behaviour of the susceptibility as a function of temperature above the Neél temperature T_N (see Eq. (1.4)) with the conclusions of the previous paragraph, we arrive at the universal thermal dependence of the susceptibility for an antiferromagnet, as schematically shown in Fig. 1.2. The temperature of the antiferromagnetic–paramagnetic transition then corresponds to the maximal susceptibility.

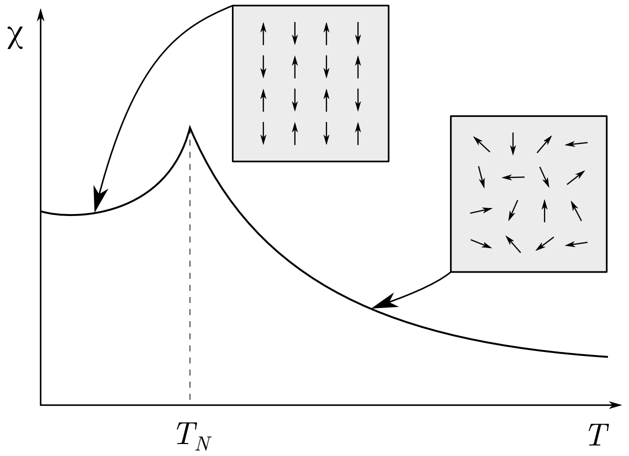

Figure 1.2: The susceptibility of an AFM as a function of temperature with highlighted antiferromagnetic and paramagnetic phases, based on [3].

1.2 Magnetotransport phenomena in antiferromagnets

In general, magnetotransport effects deal with transport properties of materials in the presence of a magnetic field. While many of these were observed, thoroughly described, and explained in ferromagnetic materials, the magnetotransport phenomena in antiferromagnets are still a subject of intensive ongoing research. In the following pages, we are going to introduce a general description of all the magnetotransport phenomena we will deal with within this thesis. Later on, we will turn our attention to antiferromagnets and their magnetotransport behaviour.

Regarding the origin of the magnetic field, we can distinguish two basic groups of magnetotransport phenomena: While for ordinary effects, the source of the field is external, anomalous magnetotransport effects arise from the existence of magnetization (or its local equivalents) in magnetically ordered materials [3].

1.2.1 Magnetoresistance

Magnetoresistance is a tendency of a material to exhibit a change of resistance R when a magnetic field $\boldsymbol{H}$ is applied. Regardless of its origin, we define magnetoresistance signal as follows:

$$MR = \frac{\Delta R}{R} = \frac{R(H) - R(0)}{R(0)}. \tag{1.5}$$

Magnetoresistance can occur in any conductive material regardless of its magnetic properties. Several types of magnetoresistant phenomena were observed, such as anisotropic MR, giant MR, or tunnelling MR. However, only anisotropic magnetoresistance (AMR) is relevant to our work, since the latter ones have been observed exclusively in layered structures [3].

Anisotropic magnetoresistance Anisotropic magnetoresistance is a magnetotransport effect which is even in magnetization. AMR signal is dependent on the orientation of magnetization with respect to the direction of the electric current $\boldsymbol{j}$ in the material (we denote the angle between $\boldsymbol{M}$ and $\boldsymbol{j}$ as ϕ; see Fig. 1.3 (a)). The signal can be decomposed into two components, crystalline and noncrystalline one. Noncrystalline AMR varies only with ϕ, whereas crystalline AMR reflects crystal symmetries through the angle ψ, which is the angle between magnetization and a reference crystalline direction. A relative change of resistance in the direction of the current flow will be called longitudinal AMR and in the perpendicular direction transverse AMR (transverse AMR is sometimes denoted as the planar Hall effect) [3]. A resistance drop due to AMR can be written for both longitudinal ΔR_{xx} and transverse ΔR_{xy} components as follows:

$$\Delta R_{xx} = r_{\mathrm{nc}} \cos(2\phi) + r_{\mathrm{c1}} \cos(2\psi) + r_{\mathrm{c2}} \cos(4\psi) + r_{\mathrm{nc,c}} \cos(4\psi - 2\phi)\,, \tag{1.6}$$

$$\Delta R_{xy} = r_{\mathrm{nc}} \sin(2\phi) + r_{\mathrm{nc,c}} \cos(4\psi - 2\phi)\,, \tag{1.7}$$

where r_{c} are coefficients corresponding to crystalline AMR, r_{nc} to noncrystalline AMR, and $r_{\mathrm{nc,c}}$ is a cross term [3]. The geometry of an AMR measurement is depicted in Fig. 1.3 (a).

While AMR in ferromagnets has been described in detail and became a textbook matter, the study of magnetoresistance in AFMs is still in its beginnings. The existence of AMR in AFMs was proposed for the first time in [8] and was later on investigated experimentally e.g. in [9].

1.2.2 Hall effects

Magnetic field applied perpendicularly to the current flow in a conductive material generates a transverse Lorenz force acting on conductive electrons, which results in a transverse Hall voltage. This is a short description of the well-known *ordinary Hall effect* [4]. In the following, however, we will focus on another phenomenon in the Hall geometry, the *anomalous Hall effect* (AHE). The AHE originates mostly in the spin-orbit interaction and is proportional to magnetization of the material.

The total Hall resistivity, which comprises a response both from the ordinary and anomalous Hall effect, can be expressed in the following manner:

$$\varrho_H = R_0\, \boldsymbol{H} \cdot \boldsymbol{n} + R_e\, \boldsymbol{M} \cdot \boldsymbol{n}, \tag{1.8}$$

where R_0 and R_e are ordinary and anomalous Hall coefficients and $\boldsymbol{n}$ is a normal to the plane of the sample (perpendicular to the direction of the current flow). The geometry of the ordinary and anomalous Hall effect is depicted in Fig. 1.3 (b) and (c).

Let us now draw our attention to the antiferromagnetic order. Although antiferromagnets have zero net magnetization, it has been demonstrated that certain noncollinear AFMs (such as $\mathrm{Mn_3Sn}$ [10]) can exhibit the anomalous Hall effect.

As stated above, the AHE arises from the spin-orbit interaction. In 2004, Bruno et al. proposed an additional component in a Hall signal originating from a topologically nontrivial spin structure, the *topological Hall effect* (THE) [11]. This effect was first reported in MnSi [12]; later, the THE was also observed in

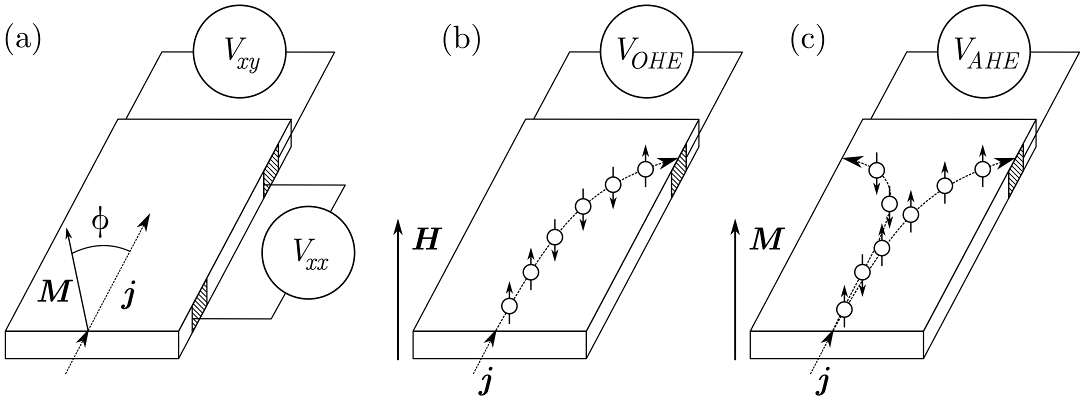

Figure 1.3: Schematic illustrations of magnetotransport phenomena. (a) Anisotropic magnetoresistance, (b) ordinary Hall effect and (c) anomalous Hall effect. In these figures, $\boldsymbol{H}$ stands for magnetic H-field, $\boldsymbol{M}$ for magnetization, and $\boldsymbol{j}$ for current density.

a noncollinear antiferromagnet Mn_5Si_3 [7] and was described theoretically for noncollinear AFM Mn_3Ge [13].

Since Hall effects are odd functions of magnetization (or magnetic field), there should not be present any Hall signal in collinear AFMs, at least none of above-mentioned variants of the Hall effect [14]. Nevertheless, a recent theoretical study of a collinear antiferromagnet RuO_2 has suggested that there is nonzero Hall response even in collinear AFMs which signal was denoted as the *crystal Hall effect* [15]. This effect results from the symmetry-breaking of the lattice due to the nonmagnetic atoms.

1.3 Thermotransport effects in antiferromagnets

Whereas the above-described magnetotransport phenomena arise from a gradient of electric potential, thermotransport effects are induced by a gradient of temperature. The symmetry of these effects closely resemble the geometry of the effects in magnetotransport, and are often described as their thermal counterparts.

In a similar way to magnetotransport, we can distinguish a thermal equivalent of magnetoresistance, thermal MR, and then the variety of counterparts to the Hall effects, so-called Nernst effects. Beyond this classification, we will also mention the Seebeck effect, which plays an important role in our measurements as an artefact.

1.3.1 Seebeck effect

The Seebeck effect is a thermoelectric phenomenon which can be in principle observed in any conductive or semiconductive material. If we apply a thermal gradient ∇T to such material, a difference in the electric potential appears that is parallel to the gradient resulting in a longitudinal voltage drop (see Fig. 1.4 (b)). The effect can be quantified by the Seebeck coefficient S as follows:

$$\boldsymbol{E}_S = S \cdot \nabla T, \tag{1.9}$$

where $\boldsymbol{E}_S$ is electric field arising from the Seebeck effect [16].

1.3.2 Magnetoresistance

Thermal AMR Thermal anisotropic magnetoresistance (tAMR) is a direct equivalent of standard AMR in a situation where a thermal gradient substitutes a gradient of electric potential. Due to the Mott relations, the Seebeck coefficient is linearly proportional to the inverse electrical conductivity $\sigma^{-1}(\boldsymbol{M})$, and thermal AMR has thus identical symmetry to AMR (see Fig. 1.4 (b)) [3, 17].

Planar Nernst effect The planar Nernst effect (PNE) can be interpreted as a thermal counterpart to the transverse component of AMR. In other words, it is a change in transverse electrical resistivity, which obeys the same angular dependence of ϕ as the transverse AMR (see Eq. (1.7)), induced by the longitudinal thermal gradient [3]. PNE is schematically described in Fig. 1.4 (b).

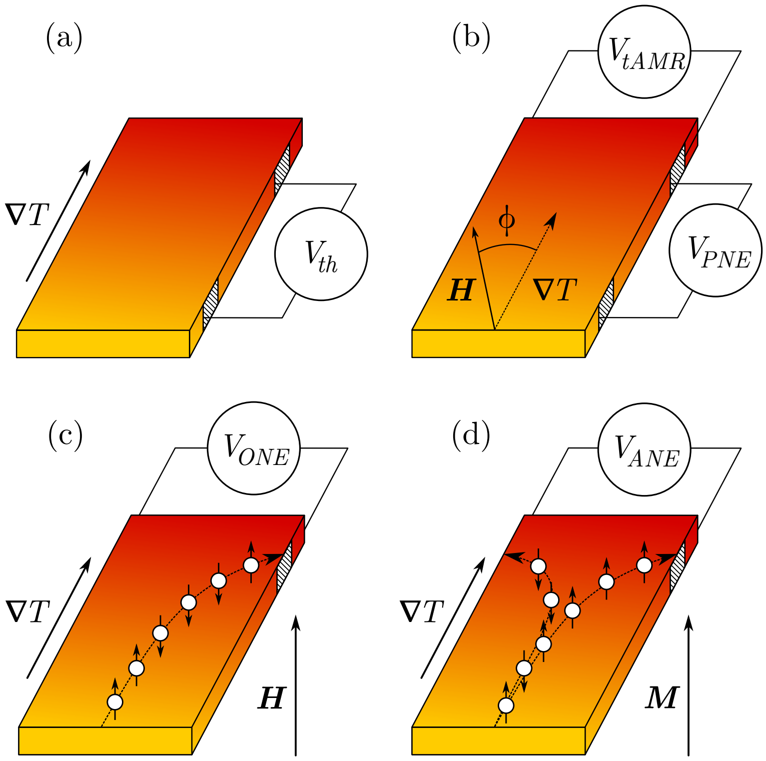

Figure 1.4: Schematic illustrations of thermotransport phenomena. (a) Seebeck effect, (b) thermal AMR and planar Nernst effect, (c) ordinary Nernst effect and (d) anomalous Nernst effect. $\boldsymbol{H}$ stands for magnetic H-field, $\boldsymbol{M}$ for magnetization, and ∇T for thermal gradient.

1.3.3 Nernst effects

As the *ordinary Nernst effect* (ONE) is a thermoelectric counterpart of the ordinary Hall effect, it also fulfils the same symmetry conditions (see Fig. 1.4 (c)): if the material is exposed to a longitudinal thermal gradient and we apply a perpendicular magnetic field, the transverse, Nernst, voltage arises [3, 18]. Similarly to the OHE, the ONE is independent of the magnetic structure and can in principle appear in any conductor (exceptionally large is in semimetals [18]). In our work, we will thus consider this signal to be parasitic and we will focus on the *anomalous Nernst effect* (ANE) which originates from the internal magnetic field (as shown in Fig. 1.4 (d)).

The overall electric field $\boldsymbol{E}_{NE}$ generated both by the ONE and the ANE can be described as follows:

$$\boldsymbol{E}_{NE} = N(\boldsymbol{B} \times \nabla T) + \alpha_{ANE}(\boldsymbol{M} \times \nabla T), \tag{1.10}$$

where $\boldsymbol{B}$ is the external magnetic field, $\boldsymbol{M}$ is magnetization (in case of ferromagnets), while N and α_{ANE} are ordinary and anomalous Nernst coefficients [18, 19].

Thermotransport phenomena in ferromagnets are a textbook matter, yet in the antiferromagnetic phase, the planar and anomalous Nernst effect have been studied just recently [3]. Two of the AFMs where the presence of the ANE has been already confirmed are noncollinear Mn_3Sn [20] and Mn_3Ge [21]. To our knowledge, no prediction or observation of a crystall-like Nernst effect in the collinear phase has been reported yet.

Chapter 2

Experimental methods and materials

In this work, we examine four samples of an antiferromagnet Mn_5Si_3 using various experimental methods in order to reveal their magnetotransport and thermotransport behaviour. In the following pages, we aim to describe the compound itself as well as lithographic structures prepared on the Mn_5Si_3 layer. Furthermore, we will introduce our experimental setups in detail.

Experimental techniques include mainly the measurement of Hall and Nernst effects, performed within the facility of the Technical University Dresden. The scanning thermal gradient microscopy was carried out in the Laboratory of Optospintronics at the Charles University.

2.1 Materials and samples

2.1.1 Mn_5Si_3

The intermetallic compound Mn_5Si_3 (mavlyanovite) is a semimetal with orthogonally distorted hexagonal structure [7, 22]. The magnetic structure of Mn_5Si_3 is highly unusual. This compound can show both collinear (cAFM) and noncollinear (nAFM) antiferromagnetic ordering depending on temperature [7].

The magnetic structure of bulk Mn_5Si_3 has been already investigated in detail by neutron scattering [7]. The Néel temperature and the temperature of the transition between the AFM states has been determined from susceptibility measurements [23]. At the Neél temperature $T_N \approx 100\,\mathrm{K}$, bulk Mn_5Si_3 undergoes a transition from paramagnetic to cAFM ordering. The magnetic structure of the collinear phase is shown in Fig. 2.1 (a): There are two groups of manganese atoms $Mn_{(1)}$ and $Mn_{(2)}$, where only $Mn_{(2)}$ atoms (two-thirds of them) show an ordered magnetic moment. These moments are oriented parallel and antiparallel to the b axis [7].

The collinear ordering persists until the temperature of $T_{cn} \approx 70\,\mathrm{K}$, where the transition to the noncollinear phase occurs. For the nAFM order, two different magnetic structures have been suggested, as shown in Fig. 2.1 (b), (c). Both magnetic configurations $nAFM_1$ and $nAFM_2$ have monoclinic symmetry, and this time also $Mn_{(1)}$ atoms exhibit an ordered magnetic moment [7].

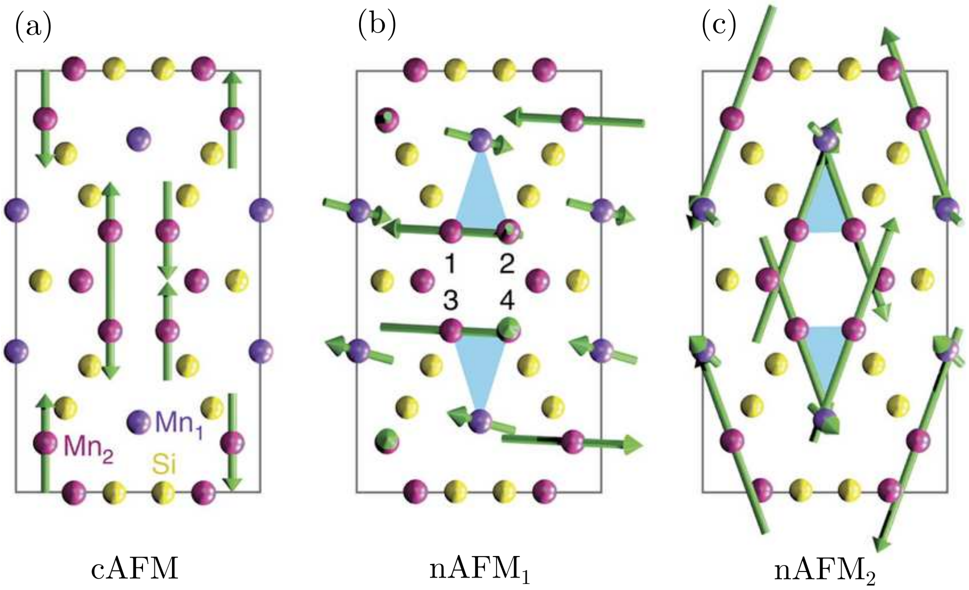

Figure 2.1: Magnetic structure of Mn_5Si_3 (view along the c axis). (a) Collinear phase cAFM, (b) noncollinear phase $nAFM_1$, and (c) noncollinear phase $nAFM_2$ [7].

2.1.2 Samples

Our experiments were performed on four samples of a thin Mn_5Si_3 layer grown on intrinsic Si(111). The growth process was done at the CINaM for all the samples. The samples come from two separate series, the first one was prepared in 2019, whereas the second one in 2020: samples from 2019 are labelled as `52` and `58`, from 2020 as `80`, and `82`. The overview of the samples is presented in Tab. 2.1. The thickness of the Mn_5Si_3 layer varies between the series: 12 nm for samples `52`, `58` and 20 nm for `80`, `82`.

sample	$\frac{t}{\text{nm}}$	devices	$\frac{w}{\mu\text{m}}$	$\frac{l}{\mu\text{m}}$	prepared at
`82`	≈ 20	2 Hall bars	≈ 10	200	TU Dresden
`80`	20	1 Nernst bar	10	250	SPINTEC
`58`	12	1 Hall bars	8	184	SPINTEC
`52`	12	1 Nernst bar	10	250	SPINTEC

Table 2.1: Overview of the samples and their properties. The table shows all the studied samples, devices used for measurement, the place where litography was performed and also their characteristic dimensions (see Fig. 2.1): t is the thickness of a Mn_5Si_3 layer, w is the width of the main channel, and l is the separation distance between the longitudinal contacts.

2.1.3 Magnetic characterization

Our work deals with Mn_5Si_3 in its antiferromagnetic phase. However, it may easily happen that during the growth process, also ferromagnetic configuration emerges. In order to ensure that there is no such phase, the magnetic state of the samples has been studied by SQUID magnetometry. A SQUID stands for a superconducting quantum interference device, which is a sensitive magnetometer enabling measurement of very weak magnetic moments and low coercive fields, and can thus distinguish a substance with no macroscopic magnetic moment from a ferromagnet. This can be accomplished by a measurement of the temperature dependence of magnetization. Fig. 2.2 shows such dependence for samples 52 and 58 measured using an in-plane magnetic field of 0.1 T. Since the measured magnetization is approximately two orders of magnitude smaller than the values typical for a ferromagnetic metal [4], we conclude that these samples do not contain any substantial amount of the ferromagnetic phase. At the time of writing, no exact results of SQUID magnetometry for samples 80 and 82 were available; yet according to the preliminary measurements, the samples seem to behave in a similar manner.

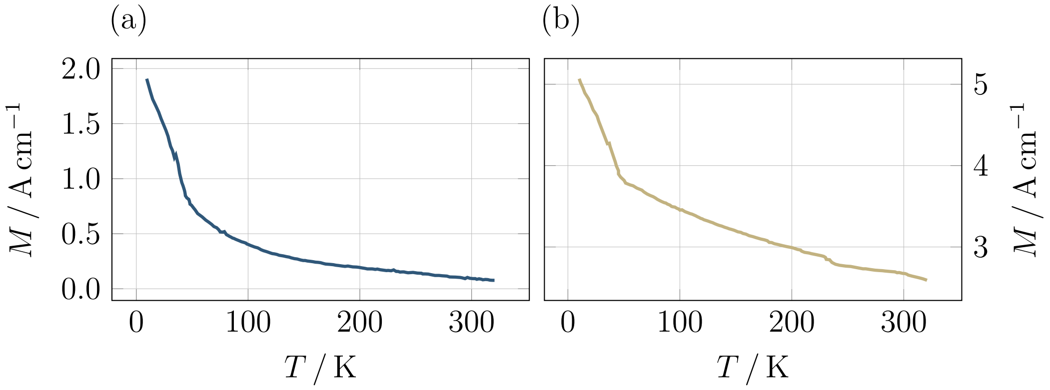

Figure 2.2: Temperature dependence of magnetization measured by SQUID magnetometry: (a) sample 52, (b) sample 58. The SQUID measurement was done using 0.1 T in-plane magnetic field.

2.1.4 Devices

In order to use the samples for transport measurements, multiple lithographic structures were prepared on the Mn_5Si_3 layer. Since the samples were used in different experiments, two types of devices were fabricated: Hall bars for the magnetotransport measurements in the Hall geometry and Hall bars with heaters (Nernst bars) for the thermotransport experiments. The lithography was done at SPINTEC and at the Technical University Dresden (see Tab. 2.1).

The Hall bar, as well as the Nernst bar, design is shown schematically in Fig. 2.3. The dimensions of the devices are not equal in all the samples (notably Hall bars on 58 and 82 differ) and are stated in Tab. 2.1. The lenght $h = 435\,\mu$m as well as $l_N = 1240\,\mu$m on Nernst bars does not vary. The Hall bars structures were prepared using only the Mn_5Si_3 layer, while the Nernst device includes also platinum components.

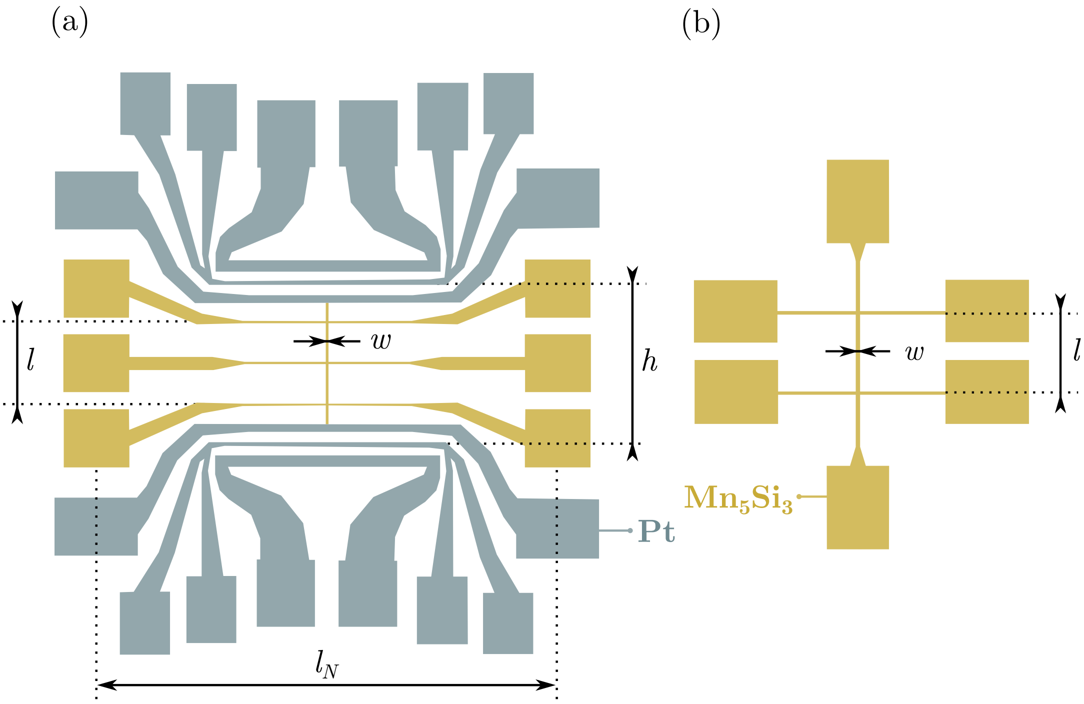

Figure 2.3: Schematics of devices used for measurements. Our samples include two types of devices: (a) Nernst bars and (b) Hall bars. The Hall bars are prepared entirely on the Mn_5Si_3 layer (yellow), while Nernst devices include also parts made from platinum (sage). Labelled dimensions correspond to values in Tab. 2.1.

2.2 Experimental methods

2.2.1 Magnetotransport measurements

The magnetotransport measurements in antiferromagnetic materials are based on a study of Hall and AMR response while manipulating with the Néel vector (ghost vector) by an external magnetic field.

As the noncollinear phase of Mn_5Si_3 emerges only at low temperatures under 70 K, the whole measurement was performed in a continuous-flow cryostat (which enables to cool the samples down from the room temperature to 5 K). The source of the external magnetic field was a superconducting vector electromagnet with a maximum field of 6 T in the z-axis and 2 T in x- and y-axes (the B-field can point in an arbitrary direction up to these limits).

The coordinate system, the orientation of the devices and the electric contact scheme are shown in Fig. 2.4. (Note that on sample 82, we have processed only data from one Hall bar which is aligned with the y-axis.) Longitudinal current has been induced by a current source *Keithley SourceMeter 2450*, while the transverse and longitudinal voltage V_{xy} and V_{xx} have been measured by a nanovoltmeter *Keithley 2182A*. In order to eliminate any signal independent of the current polarity, we have employed the gradient reversal technique: every data point was determined by subtracting signals resulting from the opposite polarities of the longitudinal current, i.e. the potential gradients (hence the name).

In our experiments, we used two measuring schemes: In the first one, the field is sequentially changing in one axis only, while the other projections are zero. From now on, we shall call these *field sweeps*. The second one, 3D *field rotations*, maintain the constant magnitude of the field while rotating its direction in xy, zy and zx planes.

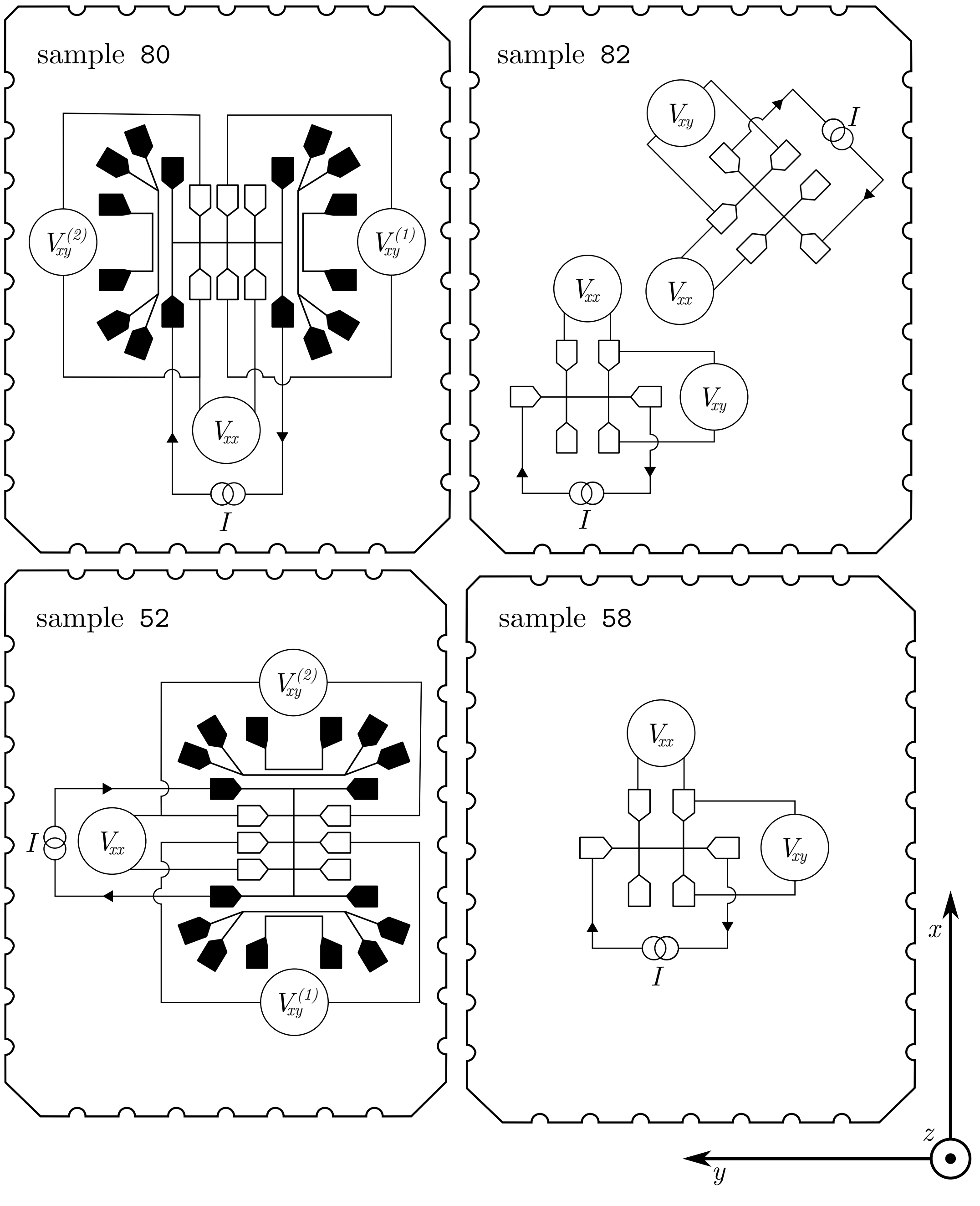

Figure 2.4: Devices for magnetotransport measurement and their electrical connection. Every panel shows devices used for the study of the Hall effects and AMR. In this type of experiment, we induce longitudinal electrical current I by a current source and measure transverse voltage V_{xy} ($V_{xy}^{(1)}$ and $V_{xy}^{(2)}$) and longitudinal voltage V_{xx}. Samples `52` and `80` are patterned to Nernst devices with three pairs of Hall contacts which enable measurement of transverse voltage on multiple contacts.

2.2.2 Thermotransport measurements

The study of the Nernst effects and thermal AMR has been performed using the same experimental setup as for the magnetotransport measurements. However, only samples `80` and `52` were patterned to the Nernst device, and merely these were employed.

A schematics of the electrical connection for both the devices is shown in Fig. 2.5. In a similar way to the magnetotransport, we measure transverse voltage $V_{xy}^{(1)}$ and $V_{xy}^{(2)}$ on two pairs of contacts as well as longitudinal voltage V_{xx} on one contact pair. Sources of in-plane thermal gradients are pairs of platinum heaters connected to the current sources I_{H1} and I_{H2}. The input power of both the heaters was 60 mW. The thermal gradient can be quantified by Pt thermometers that are directly part of the device: the thermometers are powered by the source I_T, while the voltage is read by voltmeters V_{T1} and V_{T2}.

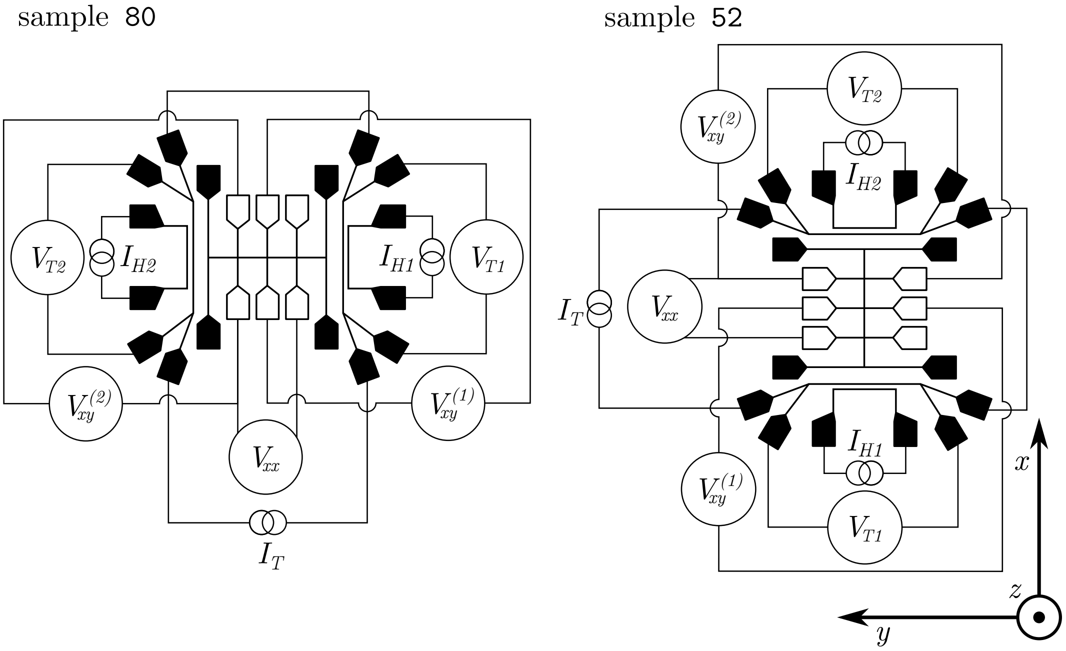

Figure 2.5: Devices for thermotransport measurement and their electrical connection for both the samples, `52` and `80`. The schematics show the detection scheme for Nernst effects and thermal AMR: Similarly to magnetotransport, we measure longitudinal V_{xx} and transverse $V_{xy}^{(1)}$ and $V_{xy}^{(2)}$ voltage; thermal gradient is induced by a pair of resistive heaters sourced by current I_{H1} and I_{H2} and quantified using a pair of thermometers (driven by current I_T) by measuring voltage V_{T1} and V_{T2}.

Again, we employ the gradient reversal method in order to remove any artefacts independent of the direction of the gradient or simply any parasitic signal not arising from thermotransport phenomena. Moreover, we eliminate any further noise by switching the polarity of the current in heaters and in thermometers and averaging the signal. One data point is then measured as follows: The direction of the thermal gradient is being changed by alternately switching on and off the heaters (see Fig. 2.6). For each such a change, polarity of the current in the heaters (of constant magnitude) is reversed. The same process is done for current in the thermometers.

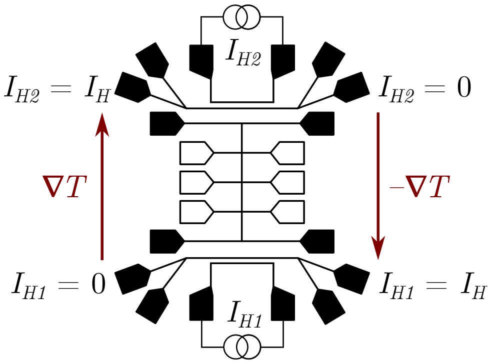

Figure 2.6: Thermal gradient reversal technique. In order to suppress any signal which does not originate in thermotransport phenomena, we switch the heaters alternately (change the current in the first heater I_{H1} to a constant value of I_H and in the second to zero and vice versa), create thus thermal gradients of an opposite direction ∇T and $-\nabla T$ and then subtract the resulting signals.

A necessary condition for quantifying thermotransport phenomena is to measure the magnitude of the temperature gradient. To do so, we have to calibrate the thermometers in the first place. The thermometers are made of platinum, and their resistance behaves linearly in most of our temperature range; however, at the lowest point of our measurement, 40 K, the nonlinear dependence starts to dominate. The calibration was performed by cooling the samples down from the room temperature to 10 K and measuring the temperature by build-in platinum sensors. For the best precision possible, we have employed cubic splines to calibrate the thermometers in the temperature range from 30 K up to 270 K. Fig. 2.7 shows the temperature dependence of resistance of the thermometers as well as a relative error between the measured dependence and its spline fit.

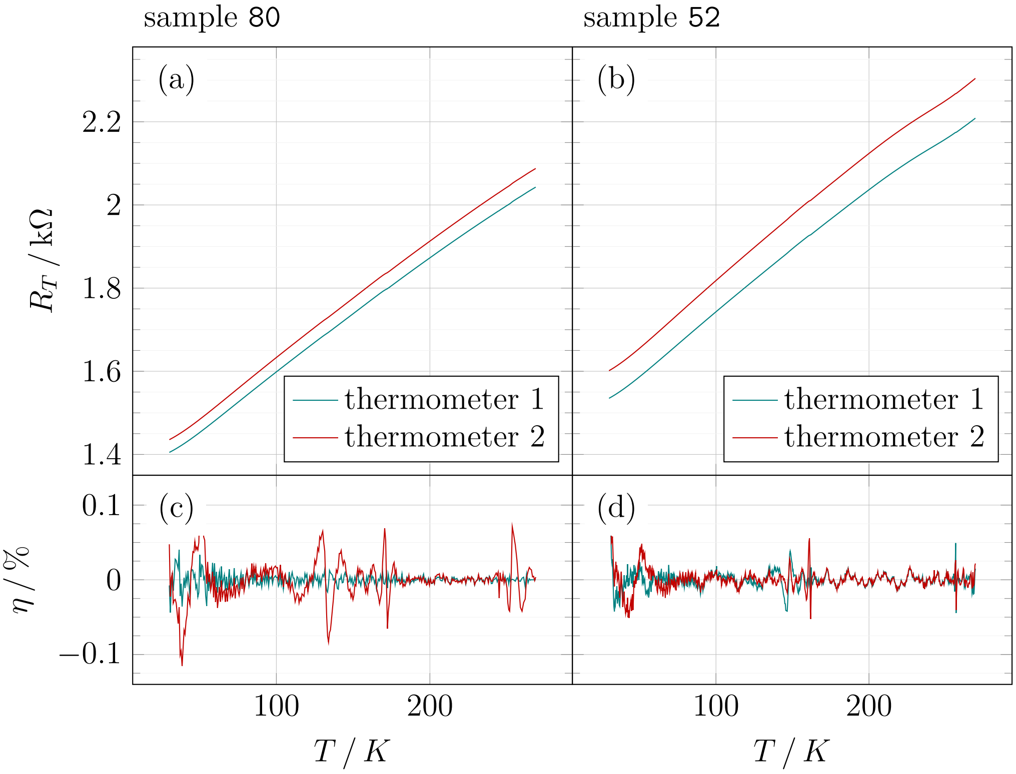

Figure 2.7: Calibration of thermometers on Nernst devices. Panels (a) and (b) show temperature dependence of the resisivity of the thermometers R_T on samples `80` and `52`. Panels (c) and (d) present a relative error η between the measured dependence and its spine calibration.

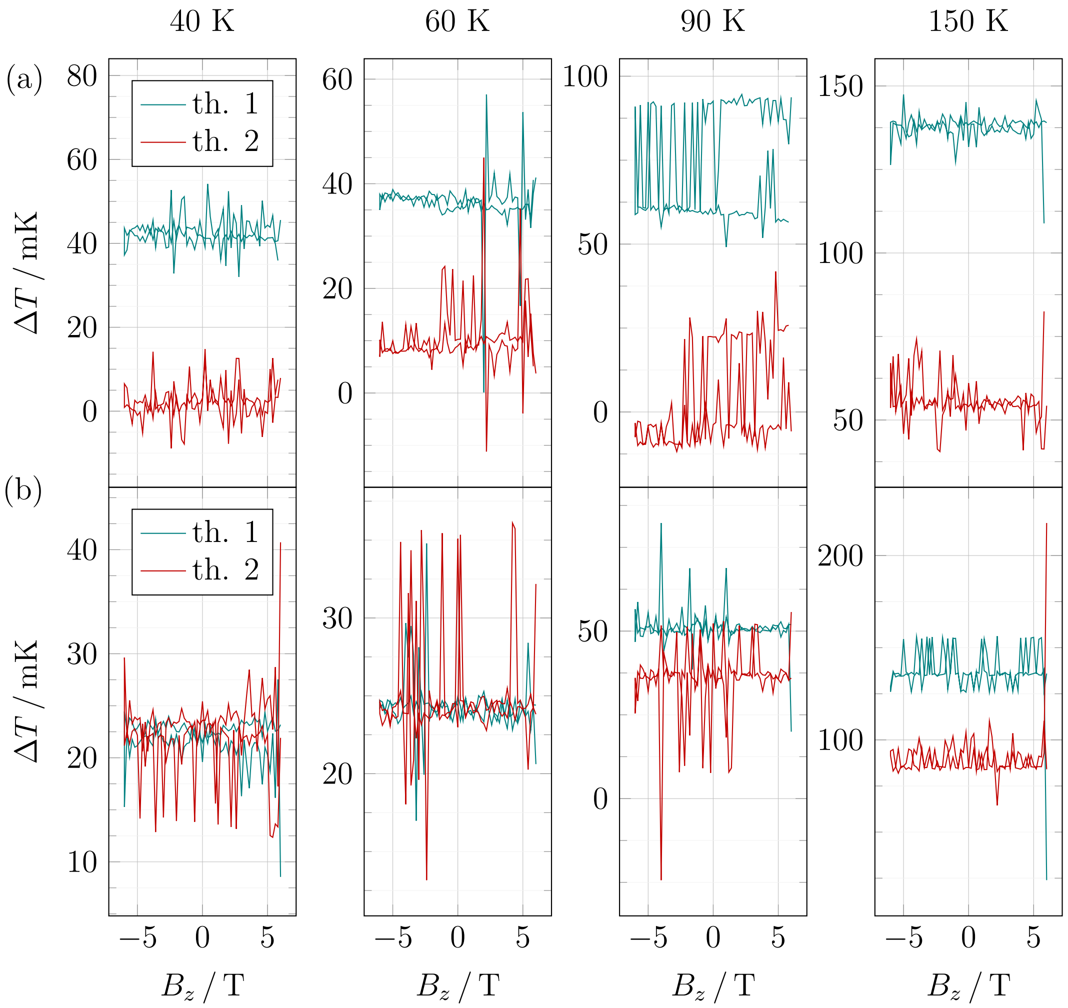

Figure 2.8: Behaviour of the temperature difference measured by the thermometers. The figure shows the temperature difference $(\Delta T)_i$, defined by Eq. (2.1), while field sweeping in z-axis for both thermometers (green thermometer 1 and red thermometer 2) on samples (a) `80` and (b) `52`.

Our thermotransport measurement included only field sweeps in the z-axis. Simultaneously with reading longitudinal and transverse voltages V_{xx} and V_{xy}, we have also measured resistance of the thermometers to estimate the magnitude of the gradient using the calibration shown in Fig. 2.7. Fig. 2.8 shows temperature difference defined as:

$$(\Delta T)_i = T_i(\nabla T) - T_i(-\nabla T) \tag{2.1}$$

where $T_i(\nabla T)$ is temperature on the first and second thermometer (T_1 or T_2) with one direction of the thermal gradient. Temperature $T_i(-\nabla T)$ has the same meaning, only the direction of the gradient is reversed. We can see that thermometers on sample `80` are highly nonsymmetric and that the reversal of the gradient induces very different change in temperature (resistance). Sample `52`, on the other hand, exhibits somewhat similar behaviour for both thermometers, at least for the temperatures under 90 K. As the induced thermal difference was in the order of magnitude of tens of milikelvins, the precision of the calibration was not sufficient to compute the thermal gradient by subtracting the temperature on both thermometers as $\Delta T = T_2(\nabla T) - T_1(\nabla T)$ (there was substantial offset between the thermometers). Therefore, we used the difference $(\Delta T)_i$ defined in Eq. (2.1) of an individual thermometer to determine the difference ΔT:

$$\Delta T = \frac{(\Delta T)_1 + (\Delta T)_2}{2}. \tag{2.2}$$

The magnitude of the thermal gradient can be then estimated as:

$$|\nabla T| = \frac{\Delta T}{h}, \tag{2.3}$$

where h is the distance between the thermometers defined in Fig. 2.3.

Because the second thermometer on the sample `80` did not seem to work correctly, in this case, we have estimated the difference only using the first thermometer. Tab. 2.2 presents the magnitudes of ∇T calculated using the temperature differences and Eq. (2.3).

samples	40 K	60 K	90 K	150 K
	$\lvert\nabla T\rvert \,/\, \mathrm{K\,m^{-1}}$			
`80`	100 ± 50	90 ± 30	160 ± 100	320 ± 100
`52`	50 ± 20	60 ± 20	100 ± 80	260 ± 200

Table 2.2: Magnitude of thermal gradient. The magnitudes of thermal gradient for Nernst devices on samples `80` and `52` were estimated using the gradient reversal method during field sweeps in z-axis. The heating power was 60 mW.

2.2.3 Scanning thermal gradient microscopy

Scanning thermal gradient microscopy (STGM) is a thermotransport technique which enables to image local magnetic structure of magnetically ordered materials. The method is based on scanning a laser spot over the sample surface. The laser spot induces locally a thermal gradient (mostly out-of plane) which, consequently, generates a thermovoltage by means of thermotransport phenomena. If the voltage independent of the magnetic order is separated, the resulting ANE signal is proportional to one projection of magnetization (or ghost vector for AFMs). By scanning the spot over the sample, we get spatial dependence of this projection and thus an image of the sample domain structure [24]. In order to manipulate with magnetization (the ghost vector), an external magnetic field can be employed. Schematic depiction of the STGM method is shown in Fig. 2.9.

Our experimental setup is introduced in Fig. 2.10. We used CW Ti:sapphire laser (*Spectra Physics 3900S*), tunable in a range of 700–1000 nm. The laser peak power was 10 mW, the wavelength was in most measurements 800 nm (partially also 725 nm and 900 nm). The laser intensity was modulated by an optical chopper at the frequency of 1 kHz in order to use a phase-sensitive (lock-in) detection technique. The beam was focused by an objective (20×, *Mitutoyo FPL NIR*) getting the FWHM of the laser spot on the sample around 2.2 μm (the measurement of the spot size using the scanning edge method is described in

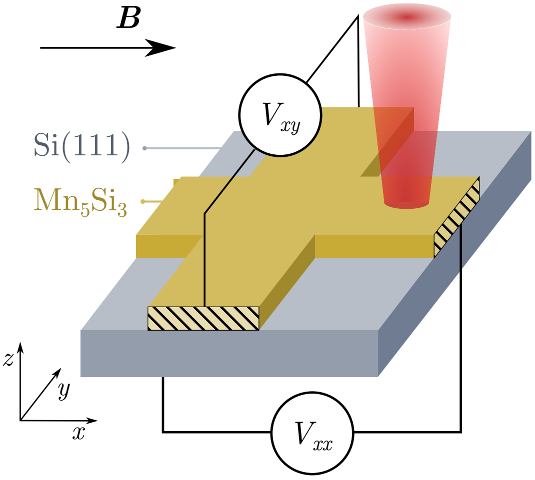

Figure 2.9: On the principle of scanning thermal gradient microscopy. The thermal gradient created by a laser beam induces both transverse and longitudinal V_{xy} and V_{xx} voltage arising from thermotransport phenomena (namely the anomalous Nernst effect). The ANE response depends on the orientation of the ghost vector $\boldsymbol{g}$ and thus on the domain structure of the sample. In order to manipulate with the $\boldsymbol{g}$ vector, a magnetic field can be applied along the x-axis.

Appx. A). The sample itself was placed in a low-vibration closed-cycle optical cryostat (*ARS Cryogenics*) between poles of an electromagnet. The magnet was oriented in the x-axis, the maximum possible field was $|\boldsymbol{B}| = B_x = 500$ mT. Using low-noise voltage preamplifier (*SRS 560*), the signal from longitudinal and transverse contacts V_{xx} and V_{xy} was pre-filtered by band pass filters set to 100 Hz/10 kHz (slope 6 dB), and amplified ten times. The resulting difference voltage is then analyzed by lock-in technique (*SRS 830*). Lock-in reference is taken from the chopper, phase is set to the signal on a device (auto phase). The beam reflected off the sample was detected either by a CCD camera or by a silicon detector. In order to locate position of the laser spot on the sample, we used a setup consisting of LED illumination (520 nm) and a CCD camera (see Fig. 2.10).

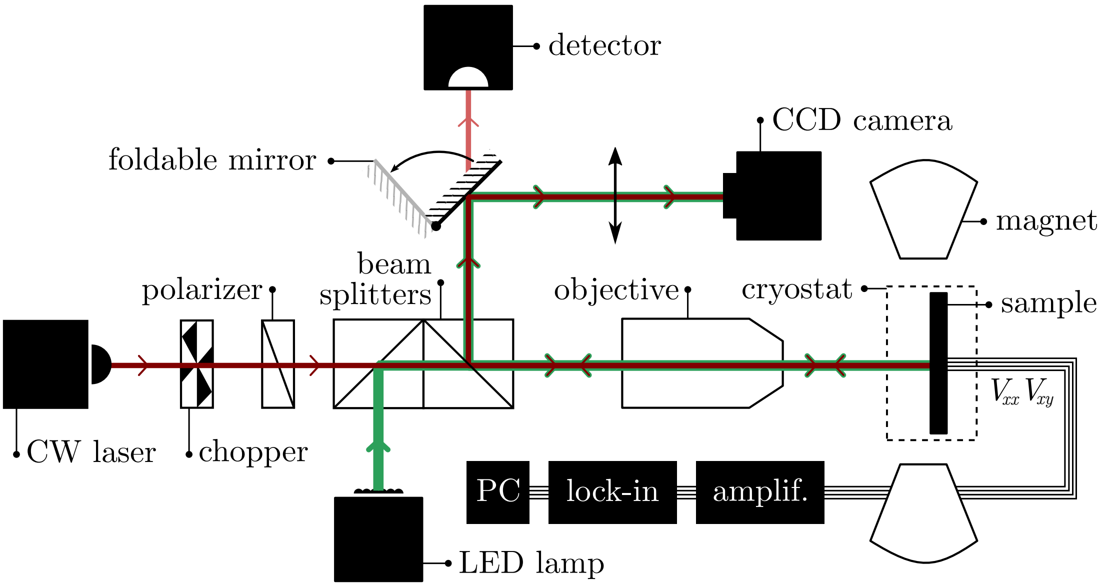

Figure 2.10: Experimental setup of a experiment using scanning thermal gradient microscopy. A foldable mirror allows switching the detection of the reflected beam between a CCD camera and a silicon detector. The path of the laser beam before entering the chopper is simplified for clarity.

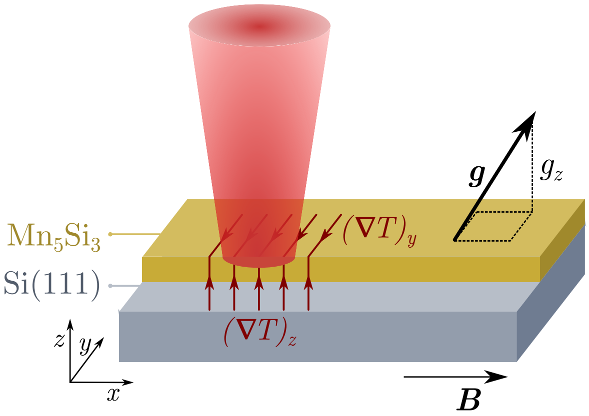

Figure 2.11: Vector quantities during scanning thermal gradient microscopy with laser beam near to the sample border. The schematics shows our understanding of the ghost vector $\boldsymbol{g}$ and the thermal gradients induced by laser beam at the edge of the sample.

Two projections of the thermal gradient induced by the laser beam can be nonzero. In every point, where the laser beam heats the sample surface, there is a projection of the thermal gradient in the z-axis $(\nabla T)_z$, as the heat is conducted to the substrate. The second nonzero component, y-component $(\nabla T)_y$, can arise in the vicinity of the borders due to the asymmetry of the in-plane gradient. The situation at the sample border is illustrated in Fig. 2.11, where the beam illuminating the edge of the device induces thermal gradients both out-of-plane $(\nabla T)_z$ and in-plane in y-direction $(\nabla T)_y$. Any Nernst response connects thermal gradient, magnetic field (either internal or external) and Nernst voltage in a way that these three quantities are perpendicular to each other (see Eq. (1.10)). Therefore, it is evident that only signal with certain symmetries can exist. In our experiment, these two contributions to the Nernst voltage can occur: Firstly, thermal gradient $(\nabla T)_y$ and the z-component of the ghost vector induce Nernst electric field along the x-axis which we can detect as the longitudinal V_{xx} voltage. And secondly, out-of-plane thermal gradient $(\nabla T)_z$ and the y-component of the ghost vector also create Nernst V_{xx} voltage and similarly, the combination of $(\nabla T)_z$ gradient and g_x cause transverse Nernst voltage V_{xy} (see Fig. 2.11).

Chapter 3

Experimental results

Our work deals with three major types of experimental design, as characterized in the previous chapter. Here we are going to describe in detail the results of these experiments and discuss the limitations of our findings.

We shall begin with the dependence of sample resistivity on temperature, as it may reflect magnetic ordering of the Mn_5Si_3 layer. Then we will continue with the magnetotransport measurements which indicate the presence of a new type of the Hall effect in the collinear AFM phase and which give us a better notion of the transition temperatures between the magnetic phases. Similarly to the magnetotransport, we will also describe thermotransport experiments which demonstrate (to our best knowledge) the first observation of the anomalous Nernst effect in Mn_5Si_3. The last part of this chapter will be dedicated to the scanning thermal gradient microscopy.

Temperature dependence of resistivity

The initial experiment was a measurement of longitudinal resistivity ρ_{xx} while cooling the sample down from room temperature (RT) to 10 K. Resistance was determined from measured longitudinal voltage V_{xx} as follows:

$$\rho_{xx} = \frac{V_{xx}}{I} \frac{t\,w}{l}, \tag{3.1}$$

where t, w, and l are dimensions of samples as stated in Tab. 2.1 and I_x is longitudinal current: we have employed $20\,\mu$A for samples 58 and 82 and $100\,\mu$A for the rest. Note that we use symbol V_{xx} for longitudinal voltage disregarding wheter it is measured along x- or y-axis. The resulting dependence of ρ_{xx} on temperature is shown in Fig. 3.1 for all samples. The figure also shows its derivative with respect to temperature $\mathrm{d}\rho_{xx}(T)/\mathrm{d}T$, which was obtained by numerical differentiation. This derivative will be crucial for our following considerations.

As described in the previous chapter, the transition temperatures between the nAFM, cAFM, and paramagnetic phases were determined in bulk Mn_5Si_3 as $T_N = 99\,\mathrm{K}$ and $T_{cn} = 66\,\mathrm{K}$. However, these temperatures can differ from the ones corresponding to Mn_5Si_3 grown in a thin layer. This is clearly visible in the following section, where we show that the anomalous Hall response can be present also above 100 K, which is the assumed Néel temperature.

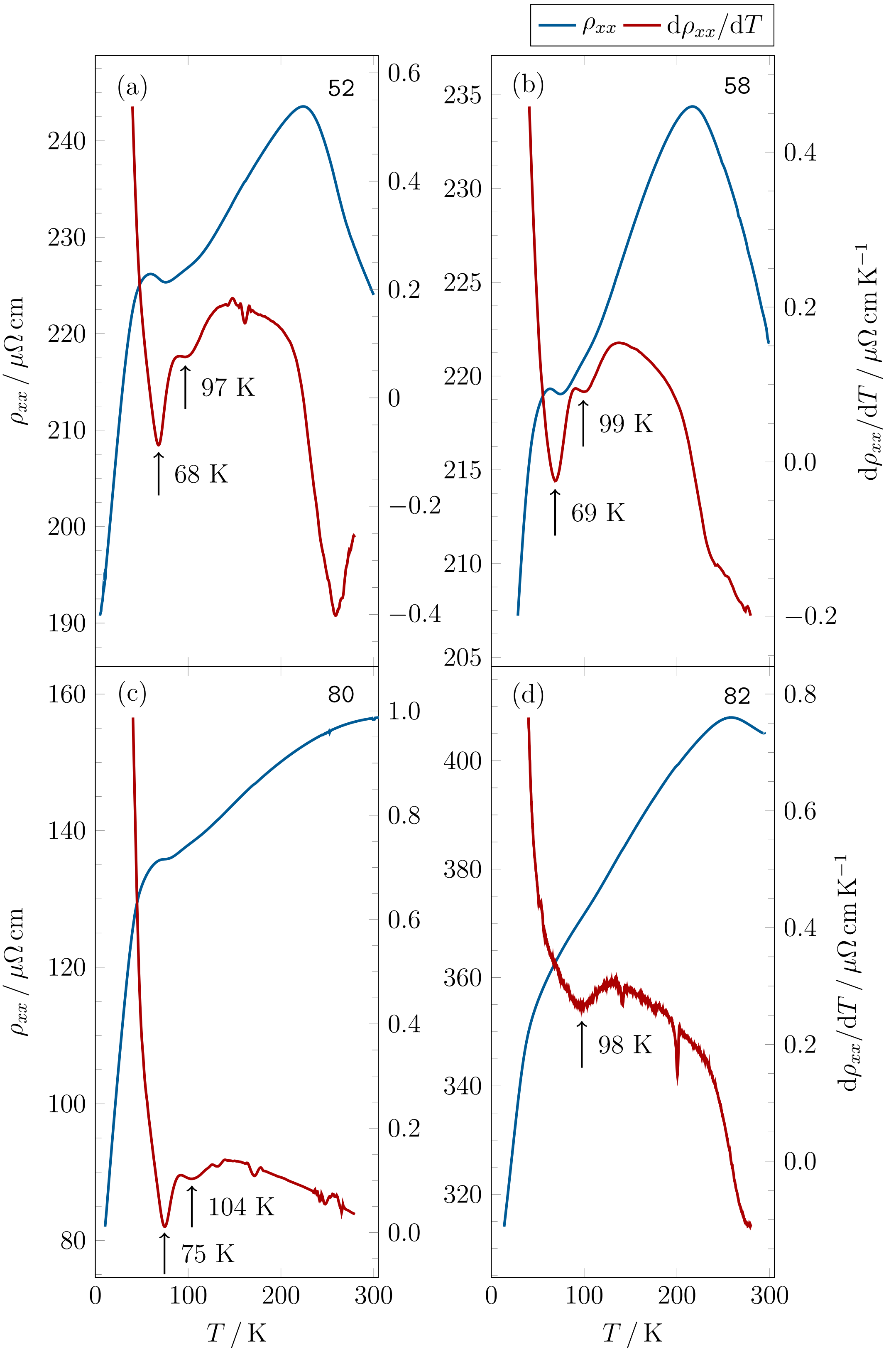

Figure 3.1: Temperature dependence of sample resistivity. The figure shows the dependence of longitudinal resistivity ρ_{xx} on temperature as well as its derivative: for sample `52` in panel (a), sample `58` in panel (b), sample `80` in panel (c), and sample `82` in panel (d). There are also pointed out the most pronounced kinks in the derivative of ρ_{xx}.

Sürgers et al. [7], who did similar experiments on a 45-nm Mn_5Si_3 film, determined the transition temperatures by corresponding kinks in the derivative of ρ_{xx} and arrived at the same values of T_N and T_{cn} as for the bulk material. We observe similar kinks in the derivative of ρ_{xx} for samples `52`, `58`, and `80` as in [7], the values of the minima are also shown in Fig. 3.1. The more pronounced kink should correspond to the cAFM–nAFM transition, while the smaller one to the Néel temperature. However, the sample `82` does not behave in a similar manner — there is only one kink near 100 K.

For the reasons that will be in discussed in detail in the following section, we are rather sceptical about using this dependence for the determination of the phase transitions. Instead, we use our magnetotransport data to estimate the temperature T_N, and, together with the thermotransport results, also to verify the T_{cn} temperature.

The last issue worth mentioning is the mutual inconsistency of the ρ_{xx} magnitudes in different samples. One can see in Fig. 3.1 that ρ_{xx} is comparable for samples `52` and `58`, however, differs substantially between samples `80` and `82`. We may remind that `52` and `58` were grown simultaneously as well as `80` and `82`, which could explain the difference between these series. However, there is also a significant variation in ρ_{xx} between `80` and `82`: the reason for that could be a different process of patterning which may have resulted in overvalued dimensions of `82` in Tab 2.1 which would then influence ρ_{xx} values through Eq. (3.1). Another considerable source of this inconsistency may be different crystalline quality (purity of the Mn_5Si_3 layer) among the samples as discussed in the following section.

3.1 Magnetotransport measurements

Our study of the magnetotransport phenomena consisted of two types of experiments. Firstly, we have employed field sweeps in the z-axis, which enabled us to observe hysteretic behaviour of transverse resistivity ρ_{xy} and magnetoresistance in the longitudinal component. The second kind, rotations of the magnetic field, gave us an insight into the orientation of the ghost vector in the nAFM phase.

3.1.1 Field sweeps

During field sweeps, we were changing the magnitude and orientation of an external magnetic field perpendicular to the sample surface (pointing in the z-axis) and we were measuring longitudinal and transverse voltage V_{xx} and V_{xy}. For all the measurements, we employed longitudinal current of $I = 100\,\mu\mathrm{A}$. The field was changed in the interval $[-6, 6]\,\mathrm{T}$ with a step of 0.4 T. We performed this set of measurements for all samples and for various temperatures between 10 K and 320 K.

The voltages V_{xx} and V_{xy} were used to calculate longitudinal and transverse resistivity ρ_{xx} and ρ_{xy}, which were the basis of our further data analysis. The longitudinal resistivity was determined using Eq. (3.1) and no further data processing was employed. Note that in the following figures, we show only the difference $\Delta\rho_{xx}$ between the longitudinal resistivity and its mean value $\Delta\rho_{xx} = \rho_{xx} - \overline{\rho_{xx}}$.

Transverse resistivity was calculated as follows:

$$\rho_{xy} = \frac{V_{xy}}{I}\frac{t\,w}{w} = \frac{V_{xy}}{I}\,t, \tag{3.2}$$

where we used the fact that the width w of the main channel is equal to the width of the transverse contacts connection. Unlike ρ_{xx}, the transverse resistivity had to be processed in order to remove artefacts arising from an improper alignment of the contacts and other types of signal distortions. For this purpose, we treated the data as presented on an example in Fig. 3.2. Panel (a) shows a raw dependence of ρ_{xy} on the magnetic field for sample 58 and temperature 10 K, as calculated from V_{xy} (an offset was removed). We anticipate that the Hall signal is an odd function of magnetic field and that the rest of the signal with different symmetry is, therefore, an artefact. Hence, we have antisymmetrized the data in panel (a) and got values presented in Fig. 3.2 (b). This curve already exhibits a pronounced hysteretic behaviour, however, it can still include artificial linear background. Finally, panel (c) shows $\rho_{xy}(B_z)$ dependence after linear background removal. This figure also defines two quantities which will play a crucial role in our following discussion: the first one is the effective coercive field $\mu_0 H_\mathrm{c}^\mathrm{eff}$, extracted as an intercept of the hysteresis loop with the $\rho_{xy} = 0$ axis, and the second one is an amplitude of the hysteresis loop P_{xy}.

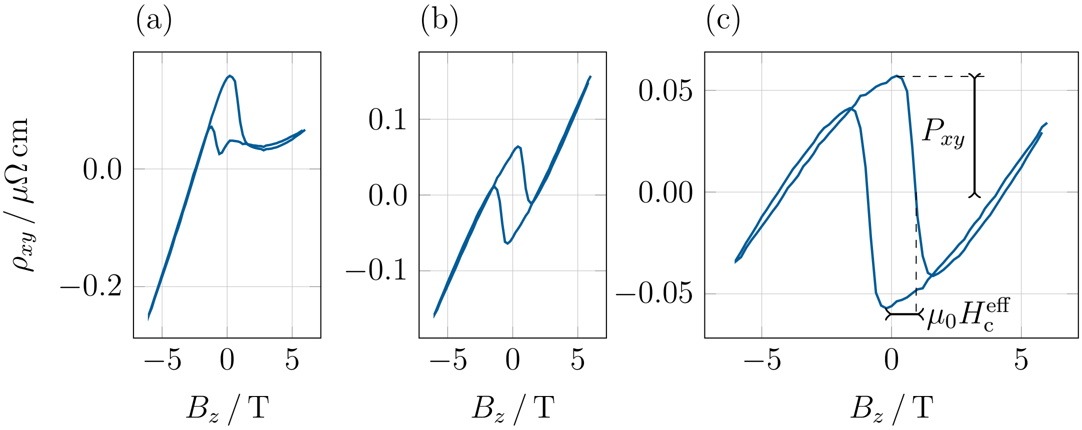

Figure 3.2: On the analysis of transverse resistance data. Panel (a) shows the dependence of transverse resistivity on B_z field as directly calculated from measured transverse voltage. In (b), the resistivity has been already antisymmetrized and in (c), a linear background has been removed. The last panel (c) also defines two quanttities: amplitude P_{xy} and the effective coercive field $\mu_0 H_\mathrm{c}^\mathrm{eff}$ that will be essential for further discussion.

For the furher analysis, we define a new quantity, transverse conductivity σ_{xy}, as follows [25]:

$$\sigma_{xy} = \frac{P_{xy}}{P_{xx}^2}, \tag{3.3}$$

where P_{xy} is the amplitude of transverse resistivity as defined in Fig. 3.2 (c) and P_{xx} is the value $\rho_{xx}(B_z = 0)$.

In the following three sections, we are going to analyze our z-field sweeps data mostly in terms of their temperature change. In the case of transverse resistivity ρ_{xy} shown in Figs. 3.3 and 3.4, we observed hysteretic behaviour which evinces three temperature-dependent regimes; these regimes also manifest in the $\Delta\rho_{xx}$ data in Fig. 3.5. Comparison of the response to z-field sweeps among the samples is shown in Fig. 3.6 which introduces temperature dependence of effective coercive field $\mu_0 H_c^{\mathrm{eff}}$, transverse conductivity σ_{xy}, and magnetoresistance $MR(6\,\mathrm{T})$. Our interpretation is depedent on the presumed magnetic state: as we also aim to estimate the transition temperatures from the magnetotransport data, please note that the following division into nAFM, cAFM, and paramagnetic phases is only approximate.

nAFM phase We shall now focus on the z-field sweeps which were performed at low temperatures below 100 K. Let us first analyze behaviour of transverse resistivity ρ_{xy} during the z-field sweeps, as shown in Figs. 3.3 and 3.4. Transverse resistivity develops hysteresis loops which, apart from the standard rectangular shape, show additional "bumps" in the vicinity of zero field (they are more pronounced above 10 K). These features persist up to the temperature of 90 K. Note that sample `82` manifests the "bumps" already at 10 K. Above 90 K, standard rectangular hysteresis is restored.

The magnitude of the hysteresis loops does not vary substantially in the whole temperature range for any sample under study. This observation is supported by Fig. 3.6 (b), where transverse conductivity indicates just a mild variation. Comparison of the samples (see Figs. 3.3 and 3.4) reveals that the values of the magnitude P_{xy} are very similar for samples `52`, `58`, and `80` — the maximum is $70-90\,\mathrm{n\Omega\,cm}$ — and approximately three times larger for sample `82` ($\approx 250\,\mathrm{n\Omega\,cm}$). However, the transverse concuctivity σ_{xy} of this sample, plotted in Fig. 3.6 (b), is comparable to the other samples. This figure also presents similarities among the samples within one series: whereas `52` and `58` shows only small change in σ_{xy} in the AFM state, there is a peak at 40 K followed by a substantial descease for samples `80` and `82`. The temperature dependence of the effective coercive field $\mu_0 H_c^{\mathrm{eff}}$ displays similar behaviour for all the samples — it is almost constant in the nAFM range (if we omit one irregular point in the characteristics for sample `52`) — yet the magnitude differs more than four times.

Let us now look at longitudinal resistivity $\Delta\rho_{xx}(B_z)$ which is presented in Fig. 3.5. This figure as well as Fig. 3.6 (c) shows that the magnetoresistence is negative in the nAFM range, peaks at 40 K and gradually decreases upon increasing the temperature, till it reaches zero in the cAFM phase. This behaviour is common for all the samples, also the magnitude of magnetoresistance is similar.

cAFM phase From the thermal dependence of longitudinal resistivity (see Fig. 3.1), we anticipate that the transition temperature to the collinear phase T_{cn} lies between 70 and 90 K. This conclusion is also supported by the x-ray diffraction and magnetic susceptibility measurements (not shown here). The same experiments also suggest that the Néel temperature T_N of our samples lies between 210 and 250 K. The cAFM phase then correspond to this temperature range ≈ 70–250 K.

The transverse resistivity during the z-field sweeps in this temperature region is depicted in Figs. 3.3 and 3.4. Even at 150 K and 200 K (210 K) there is a clear hysteretic behaviour of the signal. Moreover, the qualitative, as well as quantitative, character of $\rho_{xy}(B_z)$ is now comparable among all samples: The curves show standard rectangular hysteresis, and also the amplitudes are similar.

(a) sample 52

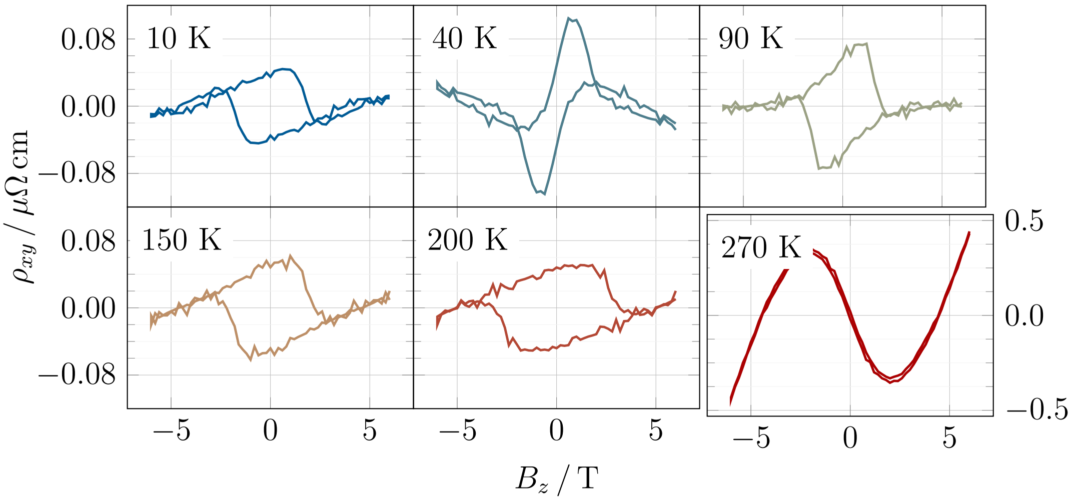

(b) sample 58

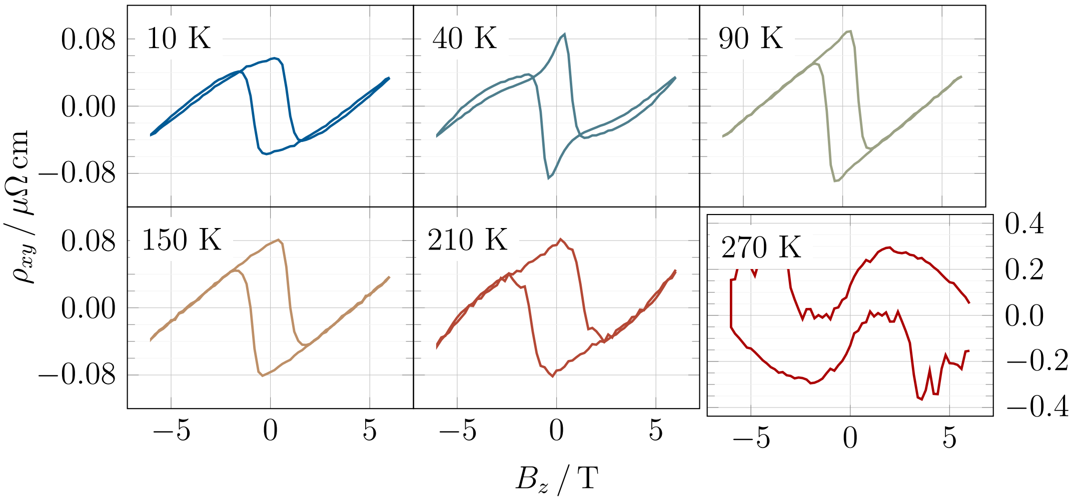

(c) sample 80

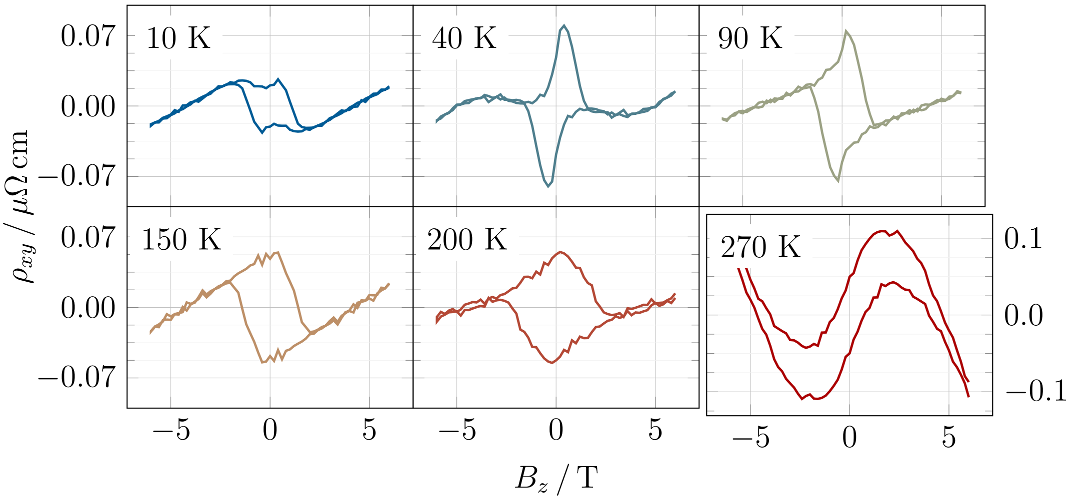

Figure 3.3: Behaviour of transverse resistance ρ_{xy} during z-field sweeps in Hall geometry for different temperatures. (a) sample `52`, (b) sample `58`, and (c) sample `80`. Note the difference in scale at 270 K.

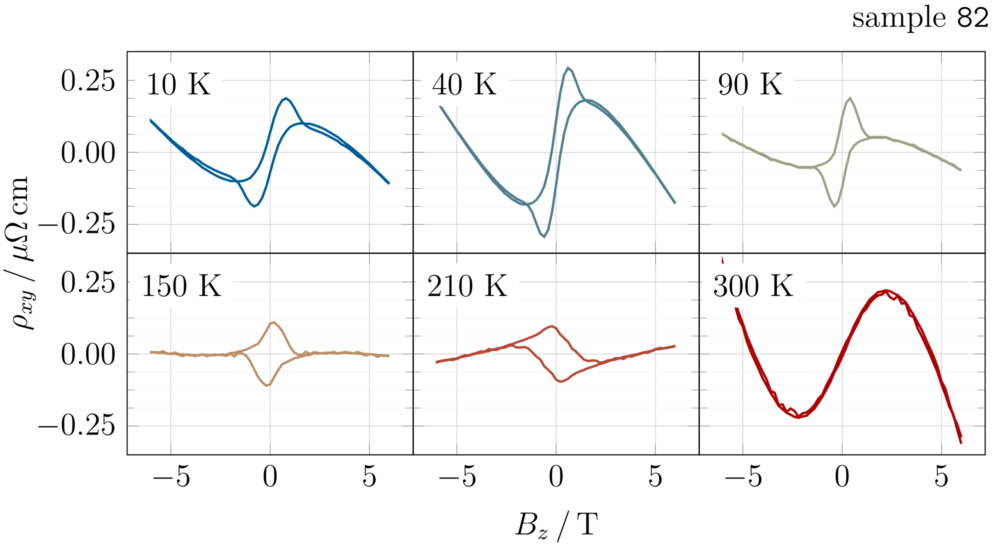

Figure 3.4: Behaviour of transverse resistance ρ_{xy} during z-field sweeps in Hall geometry for different temperatures, sample 82.

Furthermore, from the 3.6 (b) it follows that the transverse conductivity σ_{xy} has no significant temperature dependence up to 210 K, where it drops to zero. The effective coercive field $\mu_0 H_\mathrm{c}^\mathrm{eff}$ in Fig. 3.6 (a) tends to increase with temperature, peaks around 200 K and then immediatelly drops to zero. Beyond this point, the hysteretic behaviour vanishes completely.

The longitudinal resistivity has, too, very different character compared to the nAFM phase, as visible in Figs. 3.5 and 3.6 (c). The $\Delta\rho_{xx}(B_z)$ dependence exhibits a weak response to the change of the magnetic field, and magnetoresistance is virtually zero. Above 210 K, magnetoresistance starts to increase with temperature as the sample crosses the transition to the paramagnetic phase.

Paramagnetic phase There is no hysteretic behaviour in the transverse component of resistivity above 210 K, as visible in Figs. 3.3 and 3.4. Some of the figures show inconsistency while changing the field-sweep direction; however, this seems to be mostly an artefact of the measurement and data processing. Note also that the signal is substantially stronger than at low temperatures. Longitudinal resistivity in Fig. 3.5 shows a sign reversal while exceeding 210 K, and its amplitude seems to increase with temperature. Similar trend occurs in magnetoresistance in Fig. 3.6, which becomes positive in the paramagnetic phase.

From the above described, it is obvious that we see a hysteretic behaviour in all the AFM phases (below 210 K) which is in striking contrast to what has so far been known about the origin of Hall signal in antiferromagnets. In the nAFM phase (below approximately 90 K), the signal differs substantially from a standard rectangular hysteresis loop. We believe that such an anomalous shape emerges due to the mixing of two signals of different origin. The first component is, as we believe, the known topological Hall effect (THE) [7]. The THE signal in ferromagnets does not mimic the magnetization resulting in additional peaks in the vicinity of 0 T (described e.g. in [26]).

In the cAFM phase, we can see that the THE contribution disappears or decreases substantially, yet rectangular hysteretic behaviour persists. In a collinear antiferromagnet, there should be no hysteresis, as there is no established Hall mechanism which could cause such a response. A possible explanation could include the crystal Hall effect proposed in collinear AFM RuO_2 by a recent theoretical study [15]. As the name suggests, the effect results purely from the symmetry (or rather symmetry breaking) of the crystal structure. As such, the mechanism is general, it is not limited only to the collinear phase. This is demonstrated in Fig. 3.6 (b) where the transverse conductivity σ_{xy} varies just mildly between cAFM and nAFM phase. This leads us to the conclusion that the square-shaped hysteretic component of transverse resistivity in the nAFM phase (Figs. 3.3 and 3.4) also stems from the crystal Hall effect.

If we compare the behaviour of the THE for all the samples in Figs. 3.3 and 3.4, it is evident that magnitude of the bumps around zero field differs among the samples: in sample `82` it seems to be dominant signal (three times larger than for the other samples), whereas in sample `58` it is substantially less pronounced. This different behaviour can be connected to the crystalline quality (crystallinity) of the samples which plays a crucial role both for the topological and the crystal Hall effect. In our context, we understand crystallity as a measure of purity of our Mn_5Si_3 layer: During the growth process it may happen that also the ferromagnetic MnSi emerges which distorts the crystal structure. The ratio of Mn_5Si_3 and MnSi can be quantified using x-ray and it can be taken as a certain measure of crystal quality. This method indicates that the crystalline quality is highest for sample `82`, lower for `58`, then for `80`, and lowest for `52`. As this approach has been proposed just recetly, we do not show exact figures. The crystalline quality may be also reflected in Fig. 3.6 (a), where samples with higher quality show significantly lower effective coercive field $\mu_0 H_c^{\text{eff}}$.

The substantial change in the THE signal together with a drop in magnetoresistance (see Fig. 3.6 (c)) between 60 K and 90 K can be used as an independent estimate for the first AFM transition temperature. It supports our initial conclusion based on the $\rho_{xx}(T)$ dependence (Fig. 3.1) and x-ray diffraciton that the transition temperature T_{cn} is in the temperature range of 70–90 K. Similarly, complete vanishing of any hysteretic behaviour above 200 K (210 K) signifies that Mn_5Si_3 undergoes its transition to the paramagnetic state. As our measurement includes only temperatures 210 K and 250 K, we can only tell that the Néel temperature T_N lies between these points. This claim was, again, supported by the x-ray diffraction.

Field sweeps gave us a valuable insight into the temperature behaviour of magnetic ordering in Mn_5Si_3 thin layers and also into magnetotransport phenomena present in both collinear and noncollinear AFM phases. Firstly, we measured a Hall response in the nAFM phase, which we attribute to the topological Hall effect and to the recently proposed crystal Hall effect. The transition temperature between the nAFM and cAFM phases T_{cn} was estimated to be between 70 K and 90 K. Furthermore, we have detected a Hall signal in the collinear AFM phase which also originates, as we believe, in the crystal Hall effect. Finally, we used the Hall signal to estimate the Néel temperature T_N which should correspond to the temperature range between 210 K and 250 K.

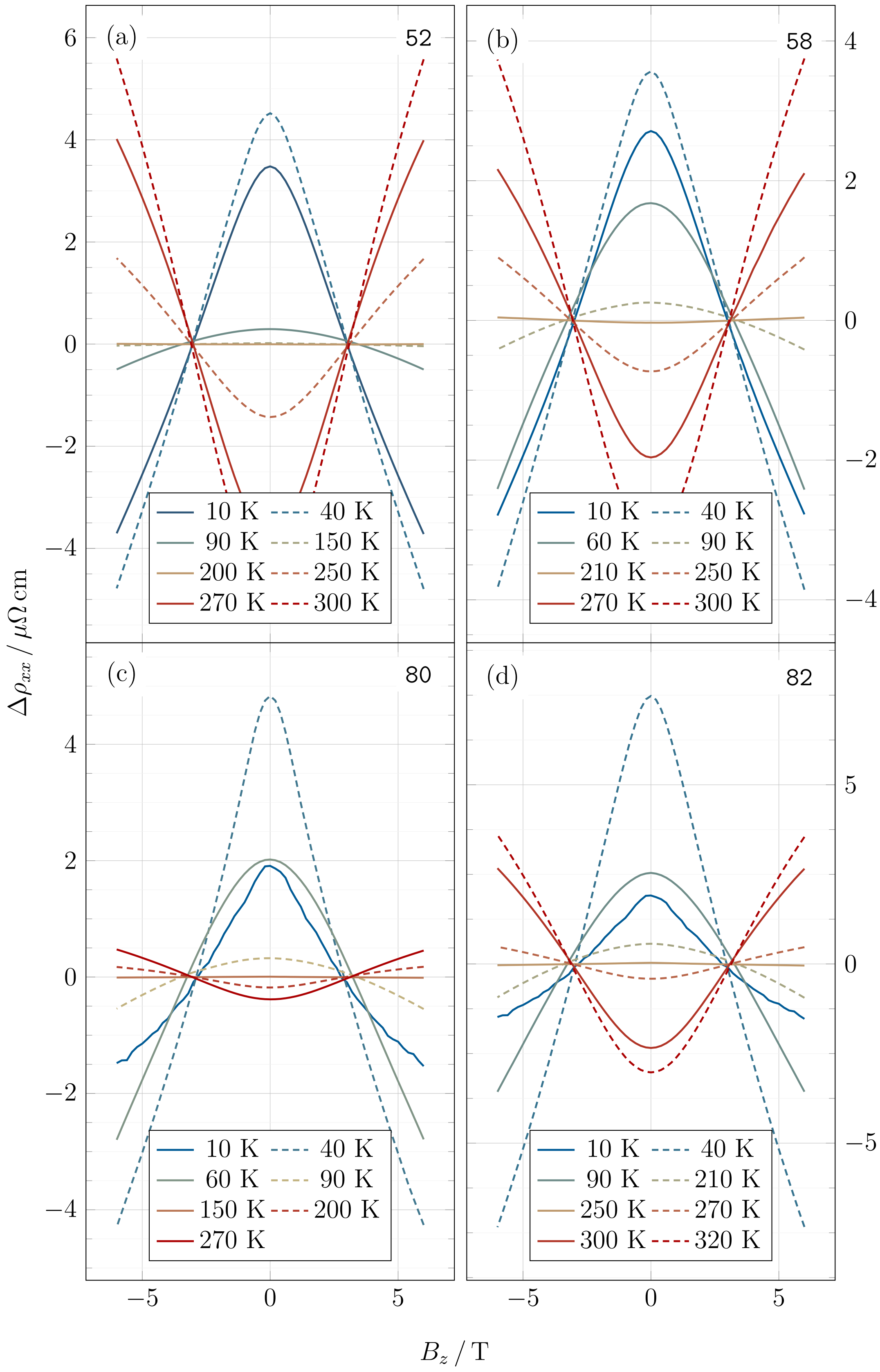

Figure 3.5: Behaviour of longitudinal resistance $\Delta\rho_{xx}$ during z-field sweeps in Hall geometry for different temperatures. (a) sample `52`, (b) sample `58`, (c) sample `80`, and (d) `82`.

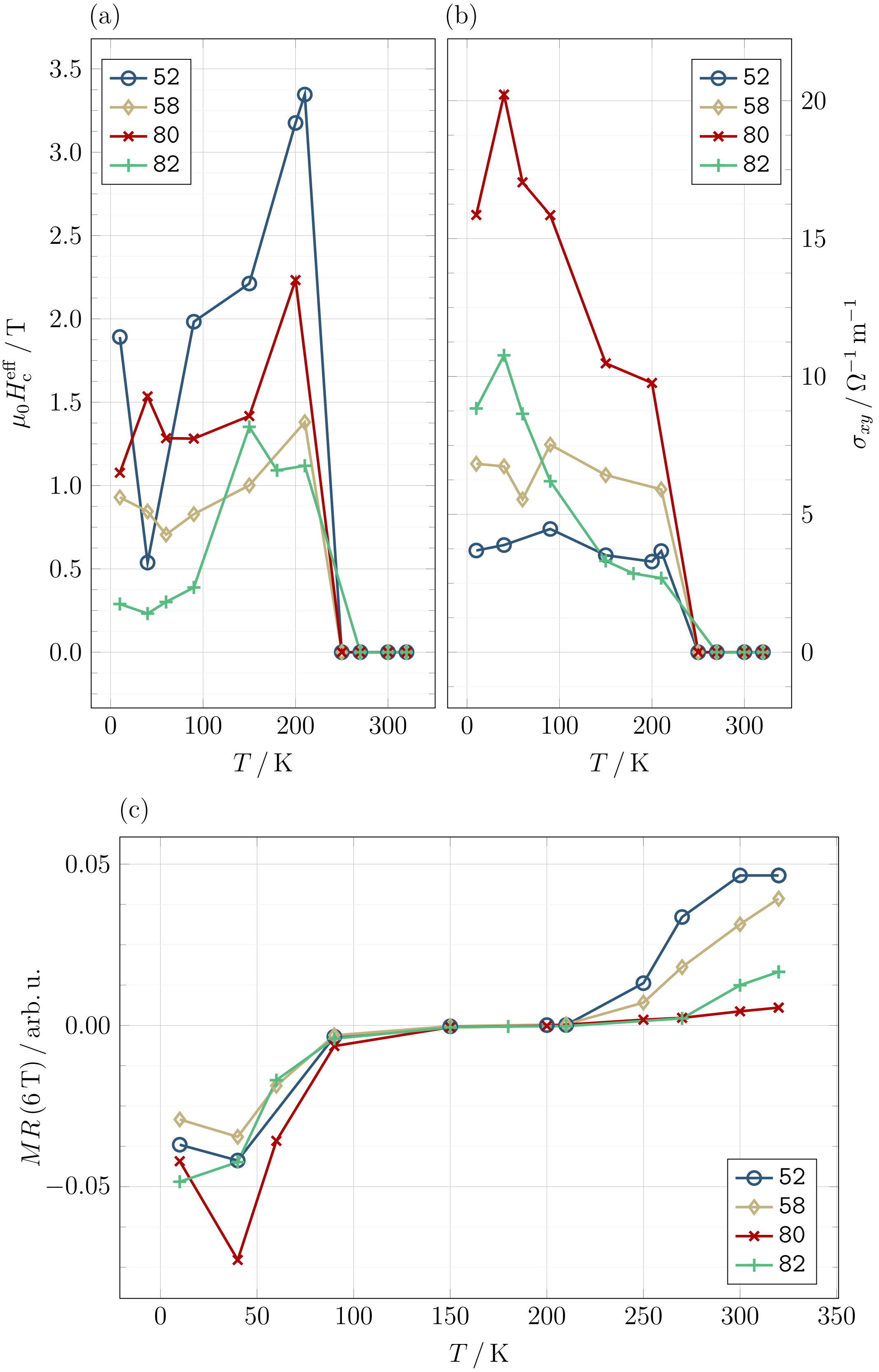

Figure 3.6: Temperature dependence of (a) the effective coercive field H_c^{eff} (introduced in Fig. 3.2), (b) transverse conductivity σ_{xy} (defined by Eq. (3.3)), and (c) magnetoresistace at 6 T $MR(6\,\mathrm{T})$ for all samples.

3.1.2 Field rotations

The second type of magnetotransport measurement employed within this thesis is the rotations of the magnetic field. During such experiment, magnitude of the external magnetic field is maintained at the constant value of 2 T, while its direction is rotated in one plane. In our measurements, we have performed the rotation for every sample in tree distinct planes: xy, zy, and zx planes (the coordinates x, y, and z were introduced in Fig. 2.4), and for two temperatures of 10 K and 150 K. Other temperature ranges will be subject of our further investigation.

Fig. 3.7 presents the dependence of transverse conductivity on the angle ϑ, which defines the direction of the magnetic field in the corresponding plane, for all the samples and above-mentioned planes at 10 K. Let us first analyze the field rotations in the xy plane. Remarkably, we measured signal which behaves like $\sim \sin 2\vartheta$ (samples `52`, `58`, and `80`) and which we consider to be a transverse component of AMR (also known as the planar Hall effect) as it has the same symmetry (see Eq. (1.7)). Transverse AMR is proportional to the sine of 2ϕ, where ϕ is the angle between the direction of the electric current and magnetization (or the ghost vector in an AFM). Our angle ϑ is the angle between the x-axis and the direction of the magnetic field, which is followed by the in-plane projection of the ghost vector $\boldsymbol{g}$. Initially, we presumed that the ghost vector points entirely out of the plane in the z-direction. The rotation in the xy plane, however, indicates that there is also significant in-plane component (at least in the samples `52`, `58`, and `80`). If the projection of the xy plane was zero, there should not be any systematic signal measured either on longitudinal or transverse contacts.

The direction of the current is shown in Fig. 2.4: in samples `58`, `80`, and `82` the current flows against the y-axis and in `52` against the x-axis. This fact also explains why the signal of `52` is shifted by 90°. In the response of sample `82` to the in-plane rotation, there is no systematic signal, and if we compare it to the response in zy and zx planes, it is substantially weaker compared with the other samples. This leads us to the conclusion that sample `82` has only a negligible in-plane component of the ghost vector.

Let us now draw our attention to the out-of-plane field rotations in the zy and zx planes, as presented in Fig. 3.7 (b) and (c). It is clear that the signal does not obey any simple periodic function, but it seems to be a mixture of at least two signals. The only exception was the sample 82 that, simultaneously, does not show any signal in the in-plane field rotation. Presumably, the first part of the signal could correspond to AMR and follows $\sim \sin 2\vartheta$. We suppose there is also the second contribution from the CHE and THE, which could not manifest in the xy rotation, as the ghost vector, current, and the contacts lie in one plane and thus do not generate any Hall response.

At 150 K, the behaviour of the out-of-plane rotation is qualitatively similar. However, there is no transverse AMR signal in the xy rotation and thus no in-plane component of the ghost vector.

The rotations of the magnetic field brought us the following conlusions: three of our samples (namely `52`, `58`, and `80`) behave at 10 K as if they had a nonzero in-plane projection of the ghost vector, while the ghost vector in sample `82` points only in the out-of-plane direction. Furthermore, there is no transverse AMR signal

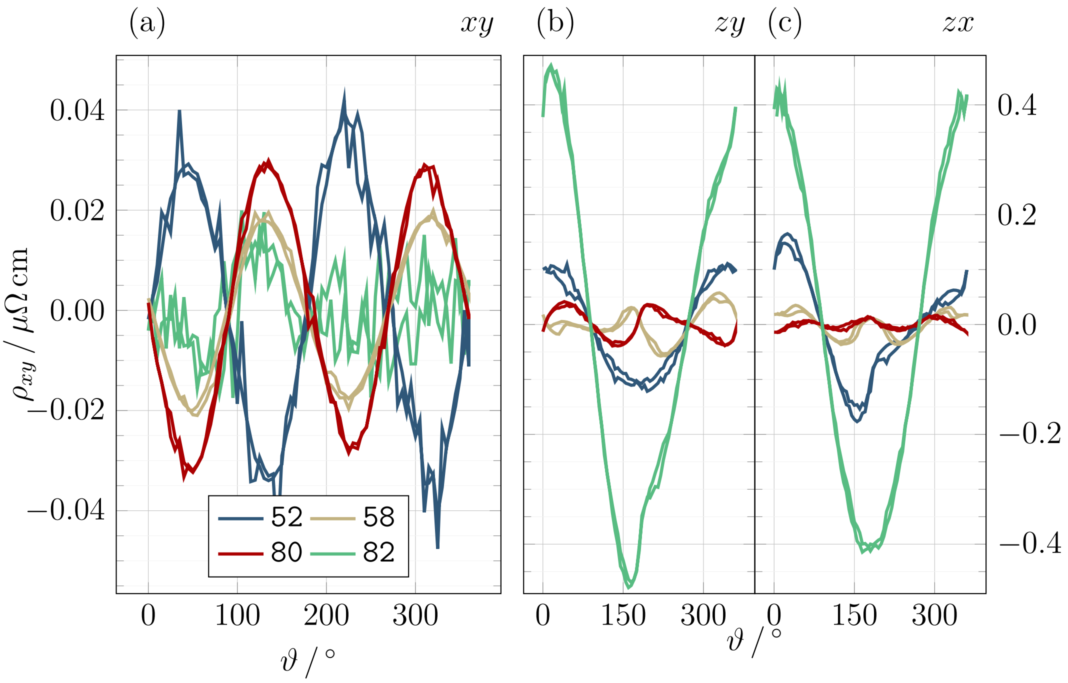

Figure 3.7: Behaviour of transverse conductivity during magnetic field rotations at 10 K in Hall geometry. The figures show how transverse conductivity ρ_{xy} varies with the direction of the magnetic field described by the angle ϑ, the magnitude of the field was 2 T. Panel (a) presents such behaviour of all samples for the rotation in the xy plane (the sample plane). Similarly, panels (b) and (c) show the $\rho_{xy}(\vartheta)$ dependence for the zy and zx plane respectively. The angle ϑ is defined by the direction of the magnetic field and by the first axis describing the plane (e.g. x-axis for the xy plane), for the coordinate system see Fig. 2.4.

at 150 K in any of the samples: either the magnetic anisotropy is different in the cAFM phase (there is no observable in-plane projection of $\boldsymbol{g}$) or the signal in the xy plane at 10 K is connected to the THE, which vanishes at higher temperatures. This observation has drawn our attention to the relationship between the signal measured during 3D rotations and the real magnetic structure of a sample. We thus propose that the transition temperatures T_{cn} and T_N could be inspected by a detailed measurement of the rotations using a fine temperature step.

3.2 Thermotransport measurements

The measurement of thermotransport properties were performed using the same experimental setup as for the magnetotransport experiments. In this case, the only method we employed were z-field sweeps. Only the samples 52 and 80 were patterned with Hall devices with heaters which enable the measurement of the Nernst effect.

The z-field sweeps included changes of the z component of the external magnetic field in the interval $[-6, 6]$ T with a step of 0.4 T. A pair of heaters induced a longitudinal thermal gradient, magnitudes of which are stated in Tab. 2.2 for both samples and various temperatures. The measurement itself was performed at temperatures of 40 K, 60 K, 90 K, and 150 K. Again, we detected transverse voltage V_{xy} and longitudinal voltage V_{xx} and used them to calculate Nernst signals S_{xy} and S_{xx}. We use the definition of the transverse signal as stated in [26]:

$$S_{xy} = \frac{V_{xy}(\nabla T) - V_{xy}(-\nabla T)}{2\, l_N\, |\nabla T|}, \tag{3.4}$$

where $V_{xy}(\nabla T)$ represents transverse voltage measured during one orientation of the temperature gradient, while $V_{xy}(-\nabla T)$ coresponds to the opposite orientation (for more details about the thermal gradient reversal technique see Sec. 2.2.2), l_N is the lenght of the transverse contact (as stated in Sec. 2.1.2), and $|\nabla T|$ is the magnitude of the thermal gradient. Longitudinal signal is defined in the same way as:

$$S_{xx} = \frac{V_{xx}(\nabla T) - V_{xx}(-\nabla T)}{2\, l\, |\nabla T|}, \tag{3.5}$$

where l is the separation distance between the contacts.

Fig. 3.8 shows the antisymmetrized S_{xy} signal with an offset removed for both samples 52 and 80 and temperatures 40 K and 60 K. We do not introduce results of the measurement at 90 K and 150 K, as these were extremely noisy and no systematic behaviour was observed. One can see that the signal for 40 K and 60 K is rather noisy as well; however, especially sample 80 shows a pronounced

(a) sample 52

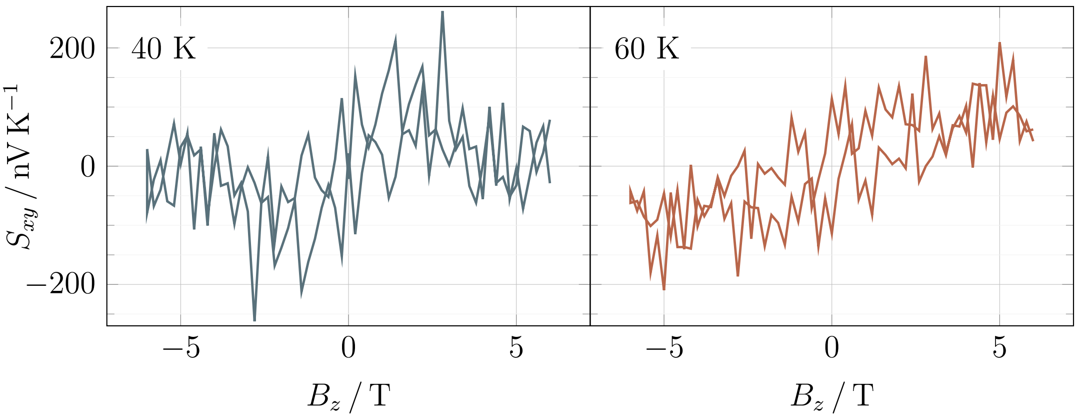

(b) sample 80

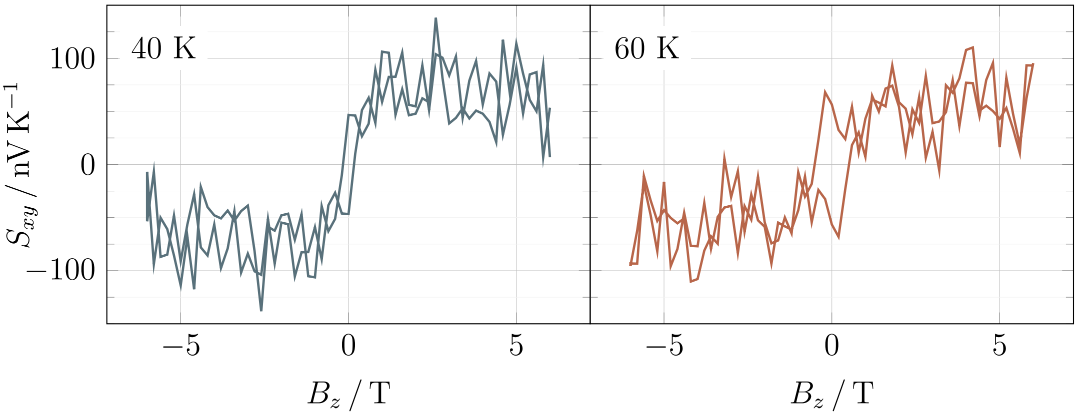

Figure 3.8: Transverse signal during z-field sweeps in Nernst geometry for 40 and 60 K. The figure shows how the quantity S_{xy} (defined by Eq. (3.4)) varies with the B_z field for (a) sample 52 and (b) sample 80 and temperatures 40 K and 60 K.

hysteretic behaviour at both temperatures, and also sample `52` suggests similar change with the magnetic field (which is very weak though). Since we have suppressed most of the possible artefacts by multiple uses of gradient reversal technique (see Sec. 2.2.2) and the hysteretic signal is apparent, we are confident to say that our S_{xy} signal originates in the current flow induced by the thermal gradient and thus that we observed a response of the anomalous Nernst effect in Mn_5Si_3. This belief is supported by Fig. 3.9 which introduces the longitudinal signal S_{xx}. Again, we can see that there is an AMR-like response which is strongest at 40 K but it is evident at 60 K as well. As there is no other source of such signal, it seems likely that the S_{xx} signal arises from the thermal AMR.

(a) sample `52`

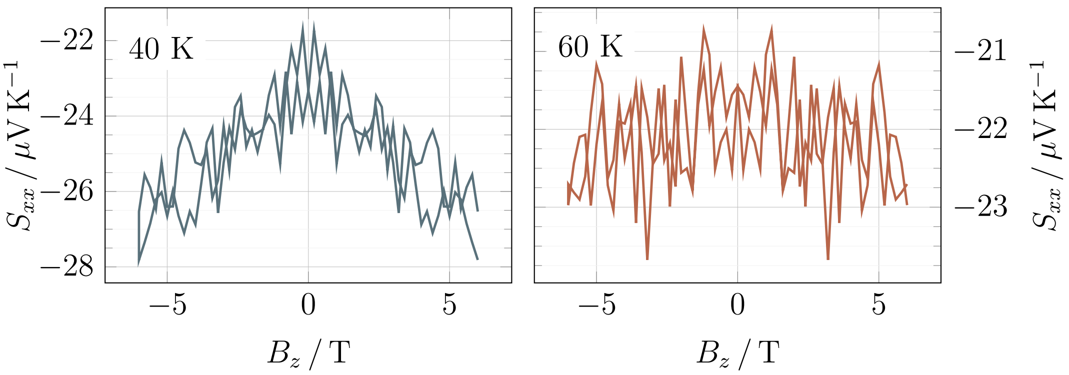

(b) sample `80`

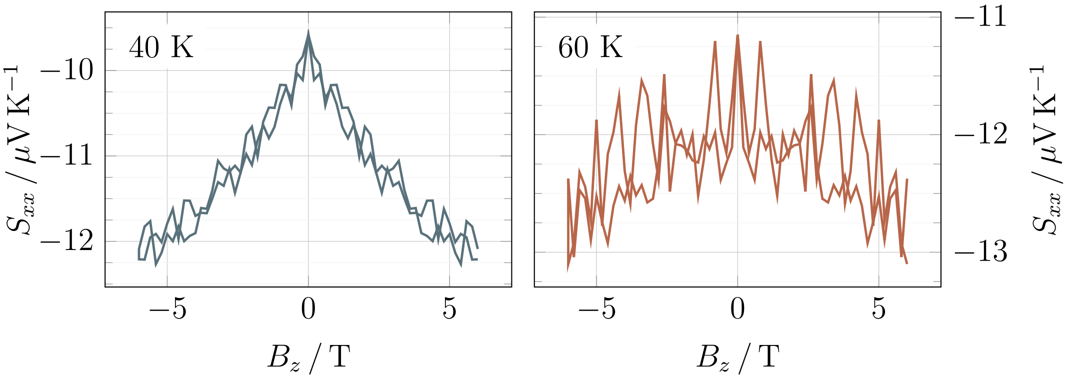

Figure 3.9: Longitudinal signal during z-field sweeps in Nernst geometry for 40 and 60 K. The figure shows how the quantity S_{xx} (defined by Eq. (3.5)) varies with the B_z field for (a) sample `52` and (b) sample `80` and temperatures 40 K and 60 K.

It is apparent that both the signals (still S_{xy} more significantly) are very weak. In order to improve the signal quality, the devices will have to be optimized in a manner which will increase the magnitude of the thermal gradient, and thus improve the Nernst response. A new device design is already under development. It will comprise heaters and a transverse contact very close together, which will enhance the gradient. This device would allow us to study the collinear phase of Mn_5Si_3 and possibly observe a new (crystal-like) type of the Nernst effect. This Nernst effect has not even been theoretically predicted; however, we observed signs of such behaviour which yet needs further investigation.

To conclude, the thermotransport measurements have revealed that there is a response of the anomalous Nernst effect in Mn_5Si_3 which has not yet been observed (to our best knowledge) in this material. Furthermore, there are promising opportunities in investigating thermotransport properties of Mn_5Si_3, as it may bring an entirely new physical phenomenon.

3.3 Thermal gradient microscopy

The last method we employed for investigation of transport properties of Mn_5Si_3 was scanning thermal gradient microscopy. The method is thoroughly described in Sec. 2.2.3; we will thus only mention important details concerning our measurement. The only sample we examined using this method was sample `80` due to certain issues which we discuss later.

As in all the previous experiments, we measured both transverse V_{xy} and longitudinal V_{xx} voltage as the laser beam was scanning over the surface of the sample. However, since we employed a phase-sensitive (lock-in) detection technique, our signal had two components: a component which was in-phase with the response in the middle of the scanning area, and the second one which was delayed by 90°. From now on, we will denote the in-phase signal as (x) and the out-of-phase one as (y), for example, $V_{xx}^{(x)}$ is an in-phase component of longitudinal voltage. We visualize these signals in the form of a map: every point corresponds to one position of the beam (our step was $0.4\ \mu$m, the data were smoothed). In the following figures, we also depict borders of the sample by a black dashed line. The borders were determined from the measurement of the reflected beam intensity, example of which is shown in Fig. A.1 (b). The samples were covered with remains of the lithographical resist, which distorted profoundly any optical measurement. We thus did each of the following experiments on the same, well-defined area of sample `80` which was free of any such impurity.

Let us now focus on Fig. 3.10 which shows maps of both components of V_{xx} and V_{xy} voltages measured at 90 K with zero magnetic field. It is evident that components of the transverse voltage $V_{xy}^{(x)}$, and $V_{xy}^{(y)}$ do not reflect the geometry of the sample (its borders) and we thus anticipate that these signals do not arise from the Mn_5Si_3 layer. The component $V_{xx}^{(x)}$ also does not seem to reflect the borders properly. We anticipate that these signals originate in the silicon substrate, which absorbs the light strongly in our wavelength range (725–900 nm). The absorbed light is directly transferred to head that creates a thermal gradient inducing Seebeck voltage on the contacts. We deal with this possibility in the following chapter where we calculate Seebeck voltage arising in such situation analytically. These components do not vary with temperature, nor with magnetic field and they thus cannot be connected with a magnetic state of the sample. We are still unsure of what precisely causes these artefacts; however, it makes the signal unsuitable for any further analysis.

The only component which seems to be promising for further discussion is $V_{xx}^{(y)}$ voltage in Fig. 3.10 (b). We stress again that this signal is shifted by 90° compared the in-phase component and that the zero phase ((x) signal) was defined in the middle of the sample. The figure shows a weak signal in the middle, whereas the response at the borders is substantially stronger. Since this behaviour reproduces

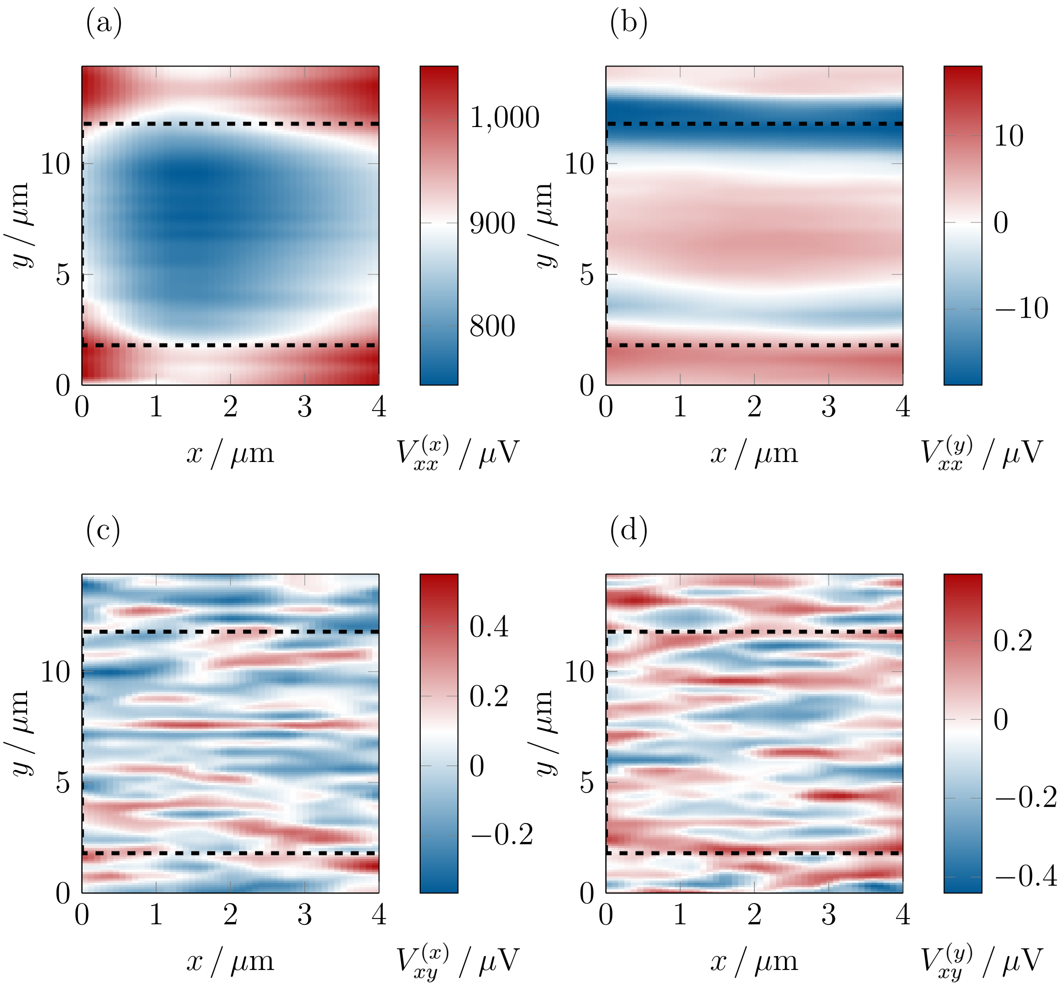

Figure 3.10: Maps of longitudinal and transverse voltages at 90 K created using scanning thermal gradient microscopy. The figure presents longitudinal and transverse voltage V_{xx} and V_{xy} measured as a laser beam was scanning over the surface of sample `80` at zero magnetic field. For both voltages, we show their components (x) which are in-phase with the signal measured in the middle of the sample and component (y) shifted by 90°. Panel (a) depicts the in-phase component $V_{xx}^{(x)}$, (b) out-of-phase $V_{xx}^{(y)}$, (c) $V_{xy}^{(x)}$, and (d) $V_{xy}^{(y)}$.

among all the measurements, we expect that this signal originates in the Mn_5Si_3 layer.

In order to reveal the source of this signal, we did the same measurement of the $V_{xx}^{(y)}$ for different values of temperature, magnetic field, and laser wavelength. The vast majority of our measurements was done using wavelength of 800 nm, however, we tested different wavelengths 725 nm and 900 nm, as shown in Fig. 3.11 for room temperature and two polarities of the magnetic field applied in the x-axis B_x. We can see that the response at both wavelengths shows border-dependent behaviour as described above. The zero phase was probably not set correctly at 900 nm, which results in shifted values and thus shifted colour scale. The signal at the borders persists also at room temperature and it is independent of the external magnetic field.

The question now is what is its cause and why we observe this response in the (y) component. When the laser beam illuminates a homogenous area, the in-plane

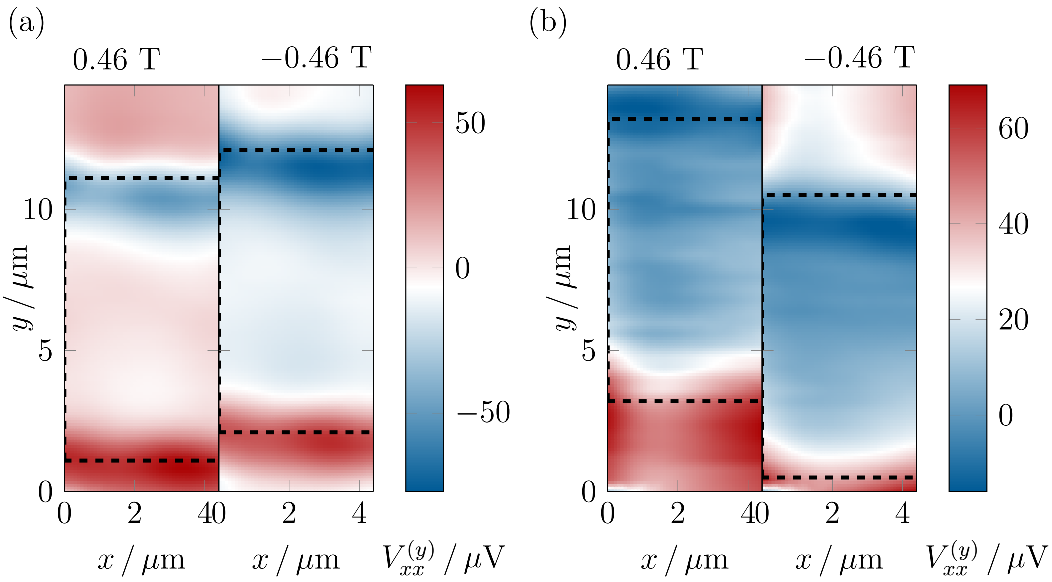

Figure 3.11: Map of $V_{xx}^{(y)}$ voltage at room temperature for both polarities of field using 725-nm and 900-nm laser. The figure captures out-of-phase component of longitudinal voltage $V_{xx}^{(y)}$ which was measured using (a) 725-nm and (b) 900-nm laser beam with magnetic field in the x-axis $B_x = \pm 0.46\,\mathrm{T}$.

thermal distribution has radial symmetry, and the in-plane thermal gradient is thus globally zero. However, if we scan with the laser beam near to the sample border, the thermal gradient becomes nonsymmetrical, and the component perpendicular to the border persists, as discussed in Sec. 2.2.3. Therefore, we assume that the signal at the borders in Fig. 3.10 (b) is connected to this perpendicular component of the in-plane gradient; however, the actual source of this signal is still unclear to us. We are confident that it does not arise from the magnetic ordering of the Mn_5Si_3 layer since we have observed this signal also at room temperature, where Mn_5Si_3 is in its paramagnetic phase.

Regarding the phase of the signal, we anticipate that the Seebeck voltage in the (x) component is dependent on the magnitude of the thermal gradient on the contacts which are far from the heated area, which causes that the (x) signal is time-shifted from the local response. This might be the reason why the signal arising locally at the borders precedes the major Seebeck signal and why we can observe it in the (y) component. There is, however, no justification for this shift to be exactly 90° and the $V_{xx}^{(y)}$ signal can be thus just a fraction of the local response. As the signal is temperature- and field-independent, we will consider it to be an artefact.

Even though the above-described signal is not induced by antiferromagnetic order of Mn_5Si_3, it corresponds to the local response and it is clearly related to the laser-induced in-plane thermal gradients. As such, we may study the Nernst response by means of this signal: We are going to investigate the behaviour of $V_{xx}^{(y)}$ voltage at low temperatures, where Mn_5Si_3 maintain magnetic order. Namely, we shall seek after any change with magnetic field which could be connected to antiferromagnetic order of the samples. To manipulate the ghost vector and to distinguish a response arising from the magnetic ordering, we employ a magnetic field along the x-axis.

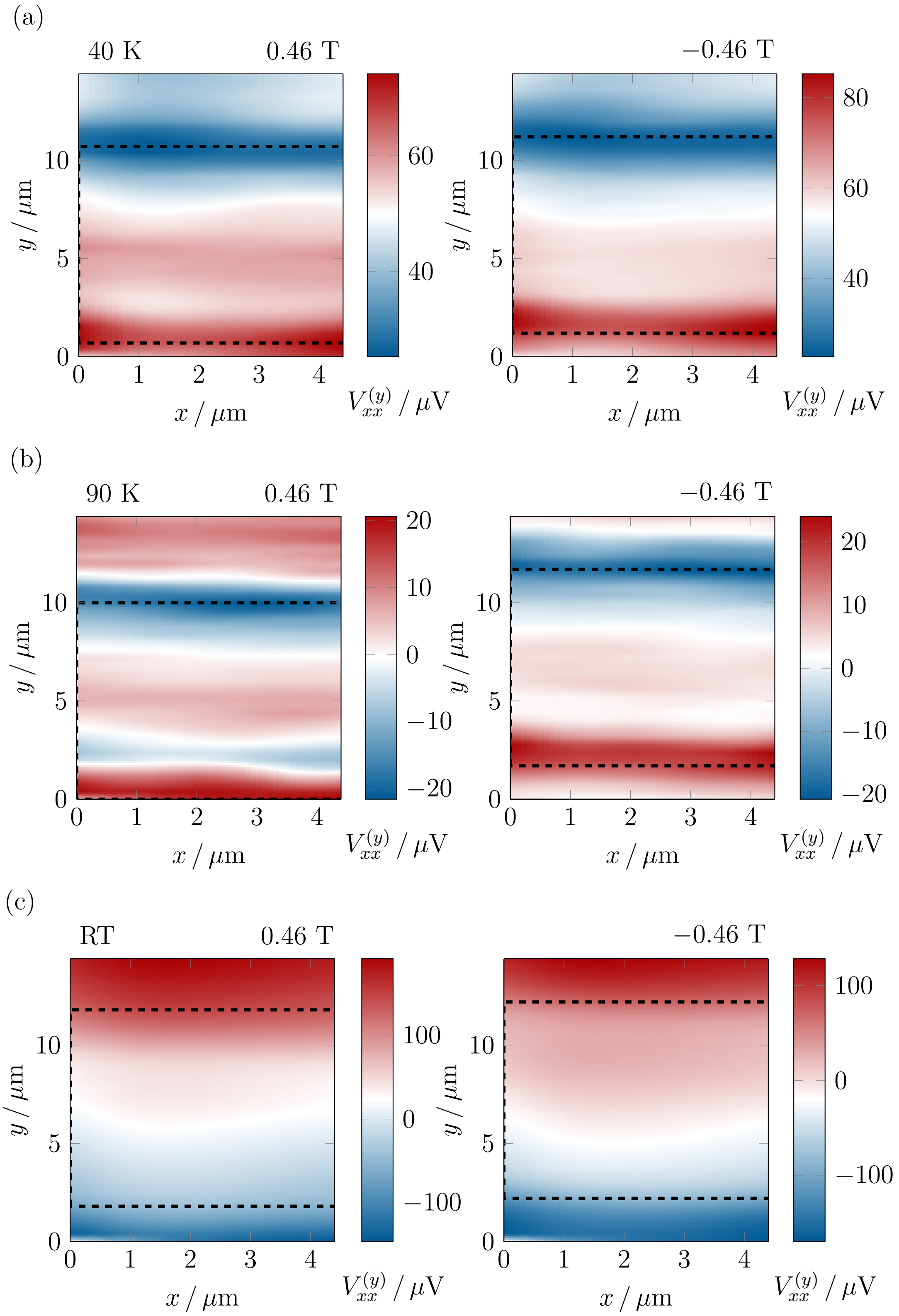

Figure 3.12: Map of $V_{xx}^{(y)}$ voltage at 40 K, 90 K, and RT for both polarities of field. We show out-of-phase component of longitudinal voltage $V_{xx}^{(y)}$ which was measured using 800-nm laser beam at (a) 40 K, (b) 90 K, and (c) room temperature for positive and negative polarity of the magnetic field along the x-axis $B_x = \pm 0.46\,\mathrm{T}$.

The maximum field we used in our measurements was $B_x = \pm 0.46\,\mathrm{T}$. Fig. 3.12 shows STGM maps at 40 K, 90 K and at room temperature for both polarities of the magnetic field $B_x = \pm 0.46\,\mathrm{T}$ and the wavelength of 800 nm. All the measurements show the same artefact at the borders as described above. However, we would like to focus on the influence of the magnetic field on our $V_{xx}^{(y)}$ signal. Fig. 3.12 (a) corresponding to 40 K does not show any substantial change between both field polarities, while panel (b), at 90 K, evince a sign change (difference in colour) at the sample lower edge. No such signal occures at room temperature which might indicate its connection to the magnetic state. In principle, the signal could be understood as follows.

If the ghost vector pointed in an arbitrary direction, we anticipate that an external magnetic field (not parallel with $\boldsymbol{g}$) inclines sligthly its direction. This would diminish or increase projections of $\boldsymbol{g}$ which causes the change in Nernst voltage that we observe. By applying positive or negative magnetic field along the x-axis $B_x = \pm 0.46\,\mathrm{T}$, we should be able to see this change in the STGM maps. We assume that the signal only shows in the vicinity of the sample border because we detect a manipulation with the z-component of the ghost vector and such signal emerges due to the in-plane thermal gradient $(\nabla T)_y$ (see Sec. 2.2.3). Since there is no substantial change at 40 K and for the above-described issues with various artefacts, we do not associate this signal directly to the Nernst response. However, this last sign of possible signal encourages us to carry on with this type of experiment.

This experimental method gave us an idea of how to progress rather than a clear physical picture. It is obvious that the silicon substrate is highly unsuitable for this type of experiments. New samples are already being prepared, which will be grown on a sapphire substrate and thus should not show such a large artefact. We also aim to optimize the shape of the devices. For this purpose, we shall use calculations introduced in the following chapter.

Chapter 4

Mathematical modelling

Measurement of thermotransport phenomena requires to generate appropriate thermal gradient. Implementation of such gradient, however, usually causes a variety of artefacts. In our work, we have employed numerical modelling in order to minimize the unwanted signal by designing the devices appropriately and also to separate the thermotransport signal from the background. Namely, we studied how an anomalous Nernst response arising from the in-plane thermal gradient is affected by the sample shape. Furthermore, we also calculated parasitic Seebeck voltage in our scanning thermal gradient microscopy (STGM) experiment.

4.1 Nernst artefacts

The first situation we are going to model corresponds to an anomalous Nernst response in a STGM experiment when the magnetic field $\boldsymbol{B}$ is perpendicular to the sample surface, and the laser beam induces an in-plane thermal gradient $(\nabla T)_{xy}$. This arrangement should reveal how the improper alignment of the

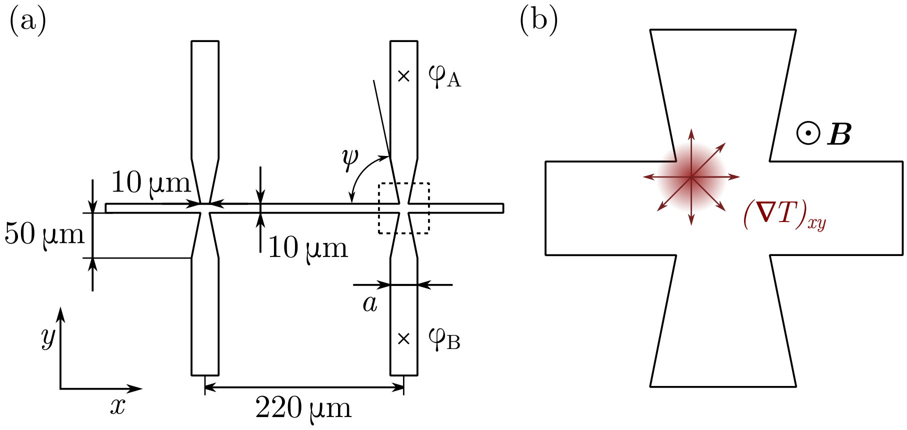

Figure 4.1: Modelling of an anomalous Nernst response in a scanning thermal gradient microscopy experiment. The figure shows (a) device we have used for our modelling, its dimensions and (b) a detail of one cross part with a marked laser spot and the corresponding thermal gradient. The magnetic field points out of the screen. Angle ψ was a free parameter, for our itinial calculations it holds that $\psi = 80°$. Transverse voltage was determined as a difference between potentials φ_A and φ_B.

sample with respect to the magnet would affect measured signal. This geometry also corresponds to our original intention to measure STGM experiments with out-of-plane magnetic field which, however, has not been done yet due to the experimental issues described in the previous chapter. Our main goal is to study how the shape of the Hall bars influences such a Nernst response.

Fig. 4.1 presents a schematic depiction of the boundaries of the sample we employed in this modelling: Panel (a) shows the whole sample, its dimensions and orientation, whereas panel (b) displays a detail of the contact crossing, the laser spot and also direction of the in-plane gradient. In order to quantify the ANE, we determined transverse voltage V_{xy} as a potential difference between the points A and B, which lie far away from the central channel.

Our model is based on the definition of electric field $\boldsymbol{E}_{ANE}$ generated by ANE (see Eq. (1.10)) and standard relations of electromagnetism. Namely, we use the following relationships: the continuity equation Eq. (4.1), no free charge considered), Ohm's law in a differential form Eq. (4.2) and also the abovementioned expression for $\boldsymbol{E}_{ANE}$ in Eq. (4.3):

$$\nabla \cdot \boldsymbol{j} = 0, \tag{4.1}$$

$$\sigma \, \boldsymbol{E} = \boldsymbol{j}, \tag{4.2}$$

$$\boldsymbol{E}_{ANE} = \alpha_{ANE} \left(\boldsymbol{M} \times \nabla T \right), \tag{4.3}$$

where $\boldsymbol{j}$ is the current density, σ is electrical conductivity and $\boldsymbol{E}$ is total intensity of electric field, which can be written as $\boldsymbol{E} = \boldsymbol{E}_{EM} + \boldsymbol{E}_{ANE}$. By combining Eqs. (4.1), (4.2), and (4.3), we get the following equalities:

$$\begin{aligned} 0 = \nabla \cdot \boldsymbol{j} = \nabla \cdot (\sigma \boldsymbol{E}) = \nabla \cdot \left[\sigma \left(\boldsymbol{E}_{EM} + \boldsymbol{E}_{ANE} \right) \right] = \nabla \cdot \left[\sigma \left(-\nabla \varphi + \alpha_{ANE} \left(\boldsymbol{M} \times \right.\right.\right. \\ \left.\left.\left. \times \nabla T \right) \right) \right] = -\nabla \sigma \cdot \nabla \varphi - \sigma \Delta \varphi + \alpha_{ANE} \nabla \sigma \cdot \left(\boldsymbol{M} \times \nabla T \right) + \sigma \nabla \alpha_{ANE} \cdot \left(\boldsymbol{M} \times \nabla T \right), \end{aligned} \tag{4.4}$$

where we use $\boldsymbol{E}_{EM} = -\nabla \varphi$. Let us denote the surface of the sample as Ω_s. In order to describe the sample and its boundaries analytically, we will use an indicator function χ_s which $\chi_s\left(x, y\right) = 1$ for all points $\left(x, y\right) \in \Omega_s$ and $\chi_s\left(x, y\right) = 0$ otherwise. We assume that conductivity $\sigma\left(x, y\right)$ is a constant σ_0 on the sample and zero outside; we can thus write $\sigma = \sigma_0 \, \chi_s$. Similarly, the same assumption holds for the coefficient α_{ANE}: $\alpha_{ANE} = \alpha_0 \, \chi_s$.

We presume that there is no current flow out of the sample boundaries. Our boundary condition is thus:

$$\boldsymbol{j} \cdot \boldsymbol{n} = \left[\sigma \left(-\nabla \varphi + \alpha_{ANE} \left(\boldsymbol{M} \times \nabla T \right) \right) \right] \cdot \boldsymbol{n} = 0 \quad \text{on } \partial \, \Omega_s, \tag{4.5}$$

where $\boldsymbol{n}$ is sample outer normal.

As we solve Eq. (4.4) using the finite element method (FEM), it is neccessary to rewrite the problem into its weak form. After multiple operations and after applying the boundary condition, we have arrived at the following weak form of the equation (4.4) with boundary condition in Eq. (4.5):

$$\int_{\Omega_s} \nabla\varphi \cdot \nabla v - \int_{\Omega_s} \alpha_0\, v\, (\boldsymbol{M} \times \nabla T) \cdot \boldsymbol{n} = 0, \tag{4.6}$$

where v is a test function. To solve this equation, we employed an FEM solver FreeFem++ (see e.g. [27]). We were interested in artefacts arising at the crossing of transverse contacts and the main channel (see Fig. 4.1 (b)) where the symmetry of the thermal gradient is significantly broken. Our computational mesh was, therefore, dense in this area and substantially sparser in the rest of the sample.

Eq. (4.6) requires to enter a particular expression for magnetization $\boldsymbol{M}$ and temperature T. We presume that the magnetization points along the z-axis only. The laser beam is expected to have a gaussian shape with FWHM $1.5\,\mu$m, and so we heuristically approximate that the temperature distribution will also be gaussian. Furthermore, it can be shown that the width (e.g. FWHM) of the gaussian thermal distribution is approximately 1.5 times larger than the beam FWHM [28]. We thus use the following form of the spatial temperature dependence:

$$T(x, y) = T_0 \exp\left[-\frac{(x - x_0)^2 + (y - y_0)^2}{2\,\sigma^2}\right] + c, \tag{4.7}$$

where c is the sample temperature without any laser heating (its value is unimportant as we use the thermal gradient only), x_0 and y_0 are the coordinates of the beam position, T_0 is the peak temperature at (x_0, y_0), and, finally, σ is a quantity proportional to the FHWM of the laser beam as $\sigma \approx \frac{1.5}{2\sqrt{2\ln 2}}$ FWHM.

As the aim of these calculations is not to quantify precisely the Nernst response, we use only approximate values of $\alpha_0|\boldsymbol{M}|$, and T_0. The anomalous Nernst coefficient of Mn_5Si_3 is not known to us. Instead, we use a rough estimate of this coefficient for bulk Mn_3Sn, which has a similar crystal structure (compare [22] and [29]). The value is $\alpha_0|\boldsymbol{M}| \approx 0.6\,\mu\mathrm{V\,K^{-1}}$ [24]. Finally, the peak temperature has been estimated to be $T_0 = 1\,\mathrm{K}$ [28].

Our calculations were done in the following manner: We have solved Eq. (4.6) using our FEM solver and subtracted transverse voltage $V_{xy} = \varphi_B - \varphi_A$ for multiple points (x_0, y_0) inside the area depicted on Fig. 4.1 (b). An example of the spatial dependence of transverse voltage $V_{xy}(x_0, y_0)$ is shown in Fig. 4.2.

Optimal shape of the devices As we would like to suppress (or at least minimize) any signal arising from the anomalous Nernst effect at the edges where the transverse contacts join the main channel, we employed two strategies for optimizing the device shape. The efficiency of our solutions was compared using a maximum of the absolute value of V_{xx} over the whole STGM map $V_{xy}^{\max}$, which we wanted to minimize.

The first strategy was to round the edges between the main channel and the transverse contacts, as shown in Fig. 4.4. We did the simulation for multiple values of the curvature radius R: the dependence of maximum voltage $V_{xy}^{\max}$ on the radius is depicted in Fig. 4.3 (a) together with an exponential fit of computed values $V_{xy}^{\max}\,/\,\mathrm{nV} = 151 \cdot \exp(-0.133\,\mu\mathrm{m}^{-1} \cdot R) + 61.1$. As expected, the parasitic voltage decreases while increasing the radius up to $15\,\mu$m. This method, rounding

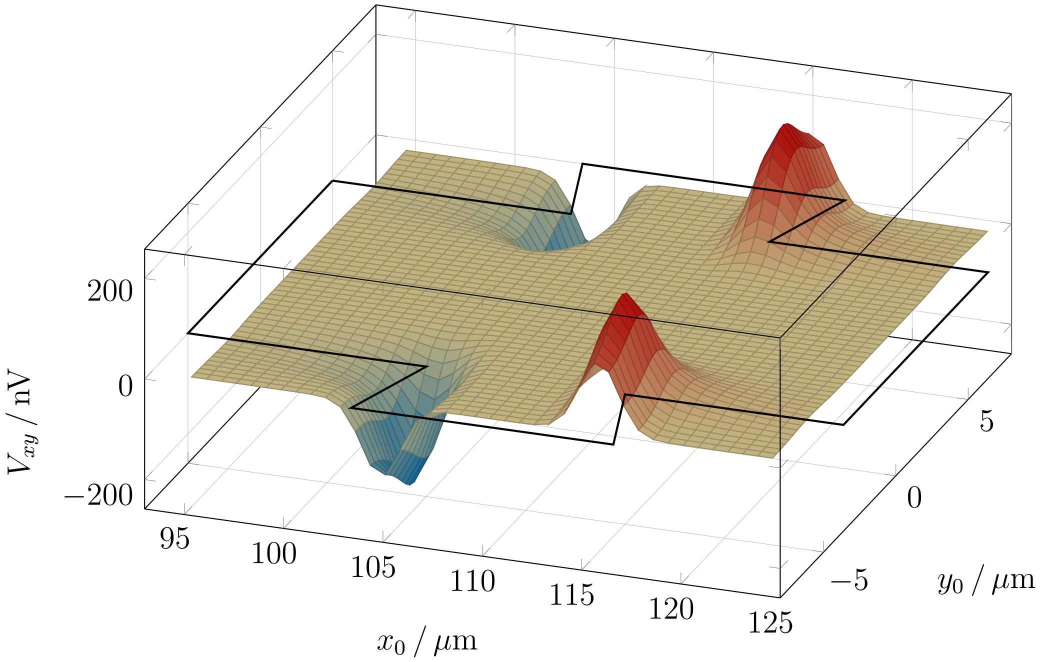

Figure 4.2: Computed map of transverse voltage generated by the anomalous Nernst effect. The figure shows the dependence of transverse voltage V_{xy} generated by the anomalous Nernst effect on the position of the laser beam (x_0, y_0). We depict only a part of the sample where the transverse contacts join the main channel. A black line represents the sample borders. (Note that the signal out of the sample border does not have any sense.)

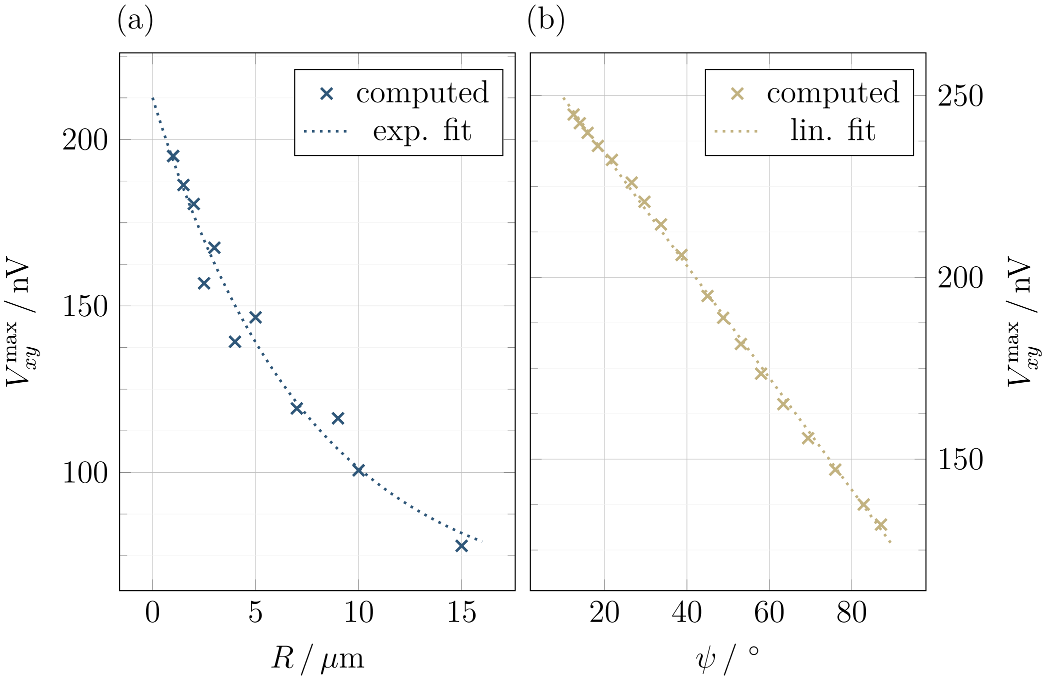

Figure 4.3: Optimization of the device shape. To quantify a parasitic Nernst response, we use voltage $V_{xy}^{\max}$ which is a maximum of the transverse voltage over our sample (its absolute value). Panel (a) shows how the voltage depends on the curvature of the device edges expressed by the radius R (which is introduced in Fig. 4.4). The dotted line is a exponential curve fitted to computed values. Panel (b) depicts a similar dependence; a variable parameter is there the angle ψ defined in Fig. 4.1 (a). The dotted line is a linear fit.

the edges, could then substantially suppress parasitic signals. It would be, however, highly impractical to fabricate devices with very round edges. The first issue would be the lithographic process itself since all standard lithographical processes allow to create only straight shapes. Secondly, such structure would prone to to mix longitudinal and transverse components of the electric field in transport measurements.

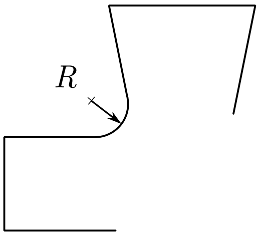

Figure 4.4: Rounding the edges of the transverse contact connection as a method for optimizing the devices. The figure indicates how we have rounded the edges of our device to suppress parasitic voltage $V_{xy}^{\max}$ and how the corresponding radius of curvature R is defined.

The second method for optimizing the lithography parameters varied the contact angle ψ introduced in Fig. 4.1 (a). We, again, observed voltage $V_{xy}^{\max}$. The change of the angle was induced by widening the dimension a (see Fig. 4.1 (a)) from the initial value of $10\,\mu$m up to $120\,\mu$m. The trend is visible in Fig. 4.3 (b): the voltage increases as the angle becomes more acute. We present there also linear fit of this dependence $V_{xy}^{\max}\,/\,\mathrm{nV} = -1.54 \cdot \psi + 265$. The optimal value is then 90°. According to this dependence, our samples were fabricated with right angles at the connections of transverse contacts.

To conclude, these simulations have shown that there is a nontrivial response from the anomalous Nernst effect in STGM measurements arising from an in-plane thermal gradient at the device borders, especially at the edges of transverse contacts. As we had performed these calculations before the sample fabrication, we could not have used our thermotransport measurements to estimate the anomalous Nernst coefficient of $\mathrm{Mn_5Si_3}$. Fig. 3.8 shows dependence of the quantity S_{xy} on a magnetic field which in the region of saturation reaches the value of approximately $70\,\mathrm{nV\,K^{-1}}$. If we consider this value to be an estimate of the anomalous Nernst coefficient (there can also be other contributions) and compare it to the value we used in our calculations $\alpha_0|\boldsymbol{M}| \approx 600\,\mathrm{nV\,K^{-1}}$, we immediately see that the computed transverse voltage in Figs. 4.2 and 4.3 is approximately nine times overestimated. Furthermore, in the next section, we show that the thermal distribution can also be calculated analytically.

This model also enabled us to determine the optimum shape of our devices which minimizes parasitic ANE signal: We have found out that less acute edges induce lower signal, and so the right angle where the transverse contacts join the main channel is desirable. Moreover, rounding the edges also leads to weaker ANE noise.

4.2 Seebeck artefacts in STGM

Our second model should clarify a very strong signal we observe in experiments using scanning thermal gradient microscopy in the longitudinal voltage $V_{xx}^{(x)}$ (see Fig. 3.10 (a)). We assume that the voltage originates in the Seebeck effect (introduced in Sec. 1.3) which arises from a thermal gradient in the silicon substrate. Since the deposited layer of Mn_5Si_3 is only tens of nanometers thick, a substantial part of the laser intensity penetrates through this layer and is absorbed in the silicon substrate. The absorbed heat then induces a thermal gradient ∇T which creates Seebeck potential difference at the contacts measured as $V_{xx}^{(x)}$.

The following equation governs the electric field induced by the Seebeck effect $\boldsymbol{E}_S$:

$$\boldsymbol{E}_S = S \cdot \nabla T, \tag{4.8}$$

where S is the Seebeck coefficient. The quantity we measure is voltage V_{xx} between the points C and D on the contacts (see Fig. 4.5). From the definition of an electric potential φ $\boldsymbol{E} = -\nabla\varphi$ and Eq. (4.8), we get an expression for transverse voltage V_{xx}:

$$V_{xx} = \varphi(D) - \varphi(C) = -S \cdot T(D) + c - (-S \cdot T(C) + c) = -S \cdot [T(D) - T(C)], \tag{4.9}$$

where c is an arbitrary constant. Hence it is evident that we have to determine the spatial distribution of temperature induced by the laser beam. To do so, we will employ the heat equation.

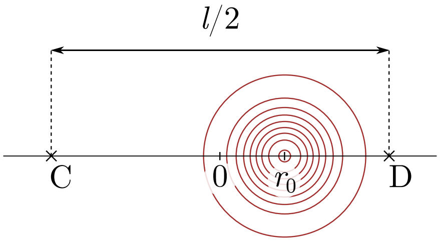

Figure 4.5: Schematics of modelling Seebeck response from silicon substrate in a scanning thermal gradient microscopy experiment. The figure depicts contacts C and D, where we measure Seebeck voltage, and their distance $l/2$. Furthermore, it shows the coordinate system and the position of the laser beam r_0.

Hereafter, we will follow the method described in [30] and we will also use the solution presented there. The procedure is based on the heat equation with a source:

$$\Delta T = \frac{C}{K}\frac{\partial T}{\partial t} - \frac{G}{K}, \tag{4.10}$$

where C is the heat capacity, K is the thermal conductivity, and G is the energy absorbed per unit volume per second. In the case of a Gaussian beam with intensity distribution $I = I_0 \exp\left(r^2/w^2\right)$ (I_0 is an amplitude), we get the following expression in cylindrical coordinates:

$$G(r,z) = \alpha(1-R)I_0 \exp\left(-\alpha z\right) I_0 \exp\left(\frac{r^2}{w^2}\right), \tag{4.11}$$

where α is the absorption coefficient (corresponds to a intensity drop to $1/e$) and R is the reflectance of silicon (we neglect the Mn_5Si_3 layer entirely).

In our model, the silicon substrate is infinite in the r-axis (the sample has several millimetres) as well as in the z-axis: the penetration depth for silicon at 77 K and for a 800-nm laser beam is approximately 20 μm [31], and the light is thus entirely absorbed in our 500- μm layer.

Since we are not interested in dynamics of the temperature distribution, we shall neglect the time dependence in Eq. (4.10) and thus we get Poisson's equation. Solution of this problem would be beyond the scope of this work, we will, therefore, use a solution for a Gaussian beam shape as described in [30]. The temperature distribution is following (note that T stands for a temperature rise to the initial temperature of the sample with no laser heating applied):

$$T(r,z) = \frac{\sqrt{\pi}\,\alpha w^2\,Q_0}{4\,K} \int_0^\infty \mathrm{J}_0\left(\frac{\xi\,r}{w}\right) \exp\left(-\frac{\xi^2}{4}\right) \frac{\alpha w \exp\left(-\frac{\xi z}{w}\right) - \xi \exp\left(-\alpha z\right)}{\left(\alpha w\right)^2 - \xi^2} \mathrm{d}\xi, \tag{4.12}$$

where J_0 is a Bessel function of zero order and $Q_0 = (1-R)I_0$ is an effective amplitude of the beam intensity. We measure voltage V_{xx} on the sample surface where $z = 0$, the integral then simplifies into:

$$T(r) = \frac{\sqrt{\pi}\,\alpha w^2\,Q_0}{4\,K} \int_0^\infty \frac{\mathrm{J}_0\left(\frac{\xi\,r}{w}\right)\,\exp\left(-\frac{\xi^2}{4}\right)}{\alpha w + \xi}\,\mathrm{d}\xi. \tag{4.13}$$

An analytical evaluation of this integral is not known; we calculated it numerically using Python library SciPy [32]. The initial temperature of the sample should correspond to our real measurements, hence to the temperature range of 40–90 K. However, not all of the properties of intrinsic Si and $\mathrm{Mn_5Si_3}$ are known at low temperatures, they have to be approximated. We use a value of the absorption coefficient in silicon $\alpha = 500\,\mathrm{cm^{-1}}$ which corresponds to the temperature 77 K [31]. Thermal conductivity of silicon at 80 K is $K = 1390\,\mathrm{W(K\,m)^{-1}}$ [33]. The FWHM of the laser beam is $1.5\,\mu$m, the corresponding width w can be determined as $w = FWHM/\left(2\sqrt{\ln 2}\right)$. The optical power was $P = 10\,\mathrm{mW}$ which is related to intensity as $I_0 = P/(\pi\,w^2)$. Finally, we consider reflectance of silicon to be $R \approx 0.33$ [34], which corresponds to 300 K. The low temperature value of R was not available, however, we do not expect any significant change since silicon does not exhibit a substantial difference ($\approx 1\,\%$) in the refractive index between 300 K and 100 K for higher wavelengths (e.g. 1 μm) [35].

Using this numerical calculation of the temperature distribution, we determined the corresponding Seebeck voltage from Eq. (4.9). Again, the value of the Seebeck coefficient in intrinsic silicon at low temperatures is unknown to us; we have therefore used the value at 380 K, which is $S = 660\,\mu\mathrm{V\,K^{-1}}$ [36]. In order to simulate our experimental setup, we compute the Seebeck response in the following manner: the laser beam moves from point C towards D, and for each position, we calculate longitudinal voltage between these two points V_{CD} (as shown in Fig. 4.5). The distance between the points is $l/2$, corresponding to the contacts in our STGM measurements (see Fig. 2.3 and Tab. 2.1). For the sample `80`, this distance is $|\mathrm{CD}| = l/2 = 125\,\mu$m. Fig. 4.5 also depicts our coordinate system: the beam position is described by a radius r_0, and since the function $T(r)$ in Eq. (4.13) is even (J_0 is even), the negative values of r_0 are defined as well. The result of our simulation is depicted in Fig. 4.6. The figure shows the dependence $V_{\mathrm{CD}}\left(r_0\right)$, which is defined as follows:

$$V_{\mathrm{CD}}\left(r_0\right) = \varphi_{\mathrm{D}}\left(r_0\right) - \varphi_{\mathrm{C}}\left(r_0\right) = -S \cdot \left[T(l/4 - r_0) - T(l/4 + r_0)\right]. \tag{4.14}$$

As we expected, the function $V_{\mathrm{CD}}\left(r_0\right)$ is odd in r_0. Our STGM measurement on sample `80` was performed in the vicinity of the contact D and its Seebeck response should thus correspond to the maximum of longitudinal voltage $\max V_{\mathrm{CD}}\left(r_0\right) \approx 0.08\,\mathrm{mV}$. A comparison of Figs. 3.10 (a) and 4.6 shows that the computed signal is approximately twelve times smaller. Reason for that could

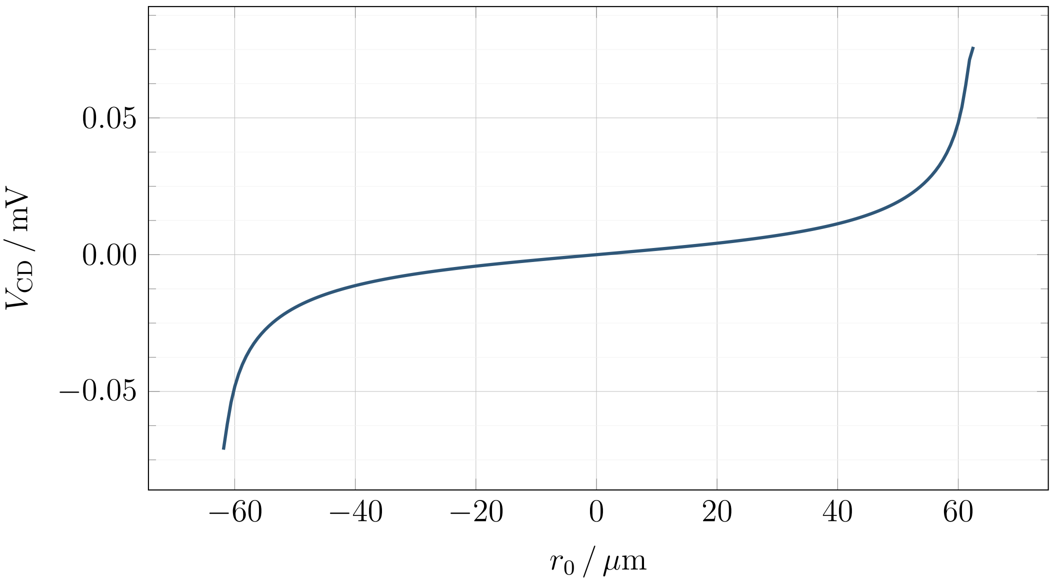

Figure 4.6: Computed dependence of longitudinal voltage induced by the Seebeck effect in silicon on the position of the laser beam. The figure shows the function $V_{\mathrm{CD}}(r_0)$ defined in Eq. (4.14), the extreme points of r_0 $\pm 62.5\,\mu$m correspond to points C and D. We consider a continuous wave of intensity 10 mW with beam FWHM 1.5 μm and the initial temperature of the sample approximately 80 K.

be our approximations (infinite dimensions of the sample) and estimated values of coefficients S and R. Furthermore, there can also be other kinds of parasitic signal such as Seebeck effect in $\mathrm{Mn_5Si_3}$, which contribute to the values we measure. On the whole, our calculations tally with the measurements done on sample `80` within the same order of magnitude.

In conclusion, this model has brought us a possible explanation of the very strong parasitic signal we have observed in the in-phase component of longitudinal voltage during scanning thermal gradient microscopy experiments. This signal can originate (at least partially) in the Seebeck effect induced in the silicon substrate. On the grounds of these observations, new samples are going to be fabricated avoiding the unsuitable silicon substrate.

Conclusion

The purpose of this thesis was to examine and describe the magnetic properties of an antiferromagnetic compound Mn_5Si_3 with a main focus on novel transport phenomena. This study was based on three distinct approaches: Primarily, it was an investigation of magnetotransport phenomena which arise from the interaction between the internal magnetic field and macroscopic electric current. Secondly, we studied thermal counterparts of these effects — thermotransport phenomena, that are induced by a thermal gradient. The scanning thermal gradient microscopy comprises the last approach, enabling to visualize the domain structure. The most significant results of this work are summarized in the following paragraphs.

The key outcome of the magnetotransport measurements is an observation of the Hall response in the collinear antiferromagnetic phase of Mn_5Si_3. According to the theory developed recently, we can attribute this signal to the crystal Hall effect resulting from the symmetry breaking by nonmagnetic atoms in the lattice. We suppose that this phenomenon also persists in the noncollinear phase at low temperatures where we observed a mixture of two Hall-like signals: most likely the responses from crystal and topological Hall effects. The correlation between these signals and the crystalline quality of our antiferromagnetic layers supports the hypothesis of their crystal-symmetry origin. The study of spatial orientation of the internal magnetic field in Mn_5Si_3 also indicates that the ghost vector can have a nonzero in-plane component, in contrast to our original expectation.

Moreover, the magnetotransport experiments helped to improve our understanding of the Néel temperature and the transition temperature between antiferromagnetic phases of thin-layered Mn_5Si_3. Whereas the latter one corresponds to the value published for bulk material, i.e. approximately 70 K, the Néel temperature is substantially higher: according to our data, it lies in the temperature range of 210–250 K.

The thermotransport measurements provided one significant physical result: the first observation of the anomalous Nernst effect in Mn_5Si_3. The Nernst signal was weak, yet clearly distinguished. Furthermore, we have observed signs of Nernst behaviour also in the collinear phase, which motivates us to continue with these measurements. Namely, we aim to design a new type of device which should substantially increase the Nernst response.

Our investigation of the Mn_5Si_3 domain structure using scanning thermal gradient microscopy gave us an idea of how to progress rather than an explicit physical result. Due to the variety of artefacts, we captured only signs of the expected Nernst response. This encourages us to prepare new samples which will be grown on different substrate.

The interpretation of the thermal maps was supported by mathematical modelling. In particular, we described the optimal shape of devices for this kind of measurement and studied the major parasitic signal originating in the Seebeck effect analytically.

To summarize, the experiments employed within this work provided us with a detailed physical picture of the magnetic ordering in Mn_5Si_3, yet there are still several questions to answer. Further research may bring a better understanding of both the Hall and Nernst effects in the collinear antiferromagnetic phase, determine the transition temperatures between the magnetic phases in Mn_5Si_3 more accurately, and describe the domain structure of thin-layered Mn_5Si_3.

Bibliography

[1] T. Jungwirth, J. Sinova, A. Manchon, X. Marti, J. Wunderlich, and C. Felser. The multiple directions of antiferromagnetic spintronics. *Nature Physics*, 14(3):200–203, 2018.

[2] L. Néel. Magnetism and the local molecular field. *Nobel Lectures, vol. Physics 1963–1970*, pages 318–341, 1970.

[3] H. Reichlová. *Nanostructures and Materials for Antiferromagnetic Spintronics.* PhD thesis, Charles University, Prague, 2016.

[4] S. Blundell. *Magnetism in Condensed Matter.* Oxford University Press, Oxford, 1st edition, 2001.

[5] J. M. D. Coey. *Magnetism and Magnetic Materials.* Cambridge University Press, Cambridge, 1st edition, 2010.

[6] J. M. Perez-Mato, S. V. Gallego, E. S. Tasci, L. Elcoro, G. de la Flor, and M. I. Aroyo. Symmetry-based computational tools for magnetic crystallography. *Annual Review of Materials Research*, 45:217–248, 2015.

[7] C. Sürgers, G. Fischer, P. Winkel, and H. v. Löhneysen. Large topological hall effect in the non-collinear phase of an antiferromagnet. *Nature communications*, 5(1):1–8, 2014.

[8] A. B. Shick, S. Khmelevskyi, O. N. Mryasov, J. Wunderlich, and T. Jungwirth. Spin-orbit coupling induced anisotropy effects in bimetallic antiferromagnets: A route towards antiferromagnetic spintronics. *Physical Review B*, 81(21):212409, 2010.

[9] X. Marti, I. Fina, C. Frontera, Jian Liu, P. Wadley, Qing He, R. J. Paull, J. D. Clarkson, J. Kudrnovský, I. Turek, et al. Room-temperature antiferromagnetic memory resistor. *Nature materials*, 13(4):367–374, 2014.

[10] S. Nakatsuji, N. Kiyohara, and T. Higo. Large anomalous hall effect in a non-collinear antiferromagnet at room temperature. *Nature*, 527(7577):212–215, 2015.

[11] P. Bruno, V. K. Dugaev, and M. Taillefumier. Topological hall effect and berry phase in magnetic nanostructures. *Physical review letters*, 93(9):096806, 2004.

[12] A. Neubauer, C. Pfleiderer, B. Binz, A. Rosch, R. Ritz, P. G. Niklowitz, and P. Böni. Topological Hall effect in the A phase of MnSi. *Physical review letters*, 102(18):186602, 2009.

[13] J. Kübler and C. Felser. Non-collinear antiferromagnets and the anomalous hall effect. *EPL (Europhysics Letters)*, 108(6):67001, 2014.

[14] J. Železný, P. Wadley, K. Olejník, A. Hoffmann, and H. Ohno. Spin transport and spin torque in antiferromagnetic devices. *Nature Physics*, 14(3):220–228, 2018.

[15] L. Šmejkal, R. González-Hernández, T. Jungwirth, and J. Sinova. Crystal hall effect in collinear antiferromagnets. *arXiv e-prints*, page arXiv:1901.00445, January 2019.

[16] K. H. J. Buschow. *Encyclopedia of materials: science and technology.* Elsevier, 2001.

[17] A. Frauen. *Magneto-Thermoelectric Effects in Co/Pt Layered Systems.* PhD thesis, Universität Hamburg, Hamburg, 2017.

[18] I. Terasaki. Thermal conductivity and thermoelectric power of semiconductors. *Reference Module in Materials Science and Materials Engineering*, 2016.

[19] I. Soldatov. *Thermoelectric effects andanisotropy in magnetic films.* PhD thesis, Technische Universität Dresden, Dresden, 2016.

[20] M. Ikhlas, T. Tomita, T. Koretsune, M.-T. Suzuki, D. Nishio-Hamane, R. Arita, Y. Otani, and S. Nakatsuji. Large anomalous nernst effect at room temperature in a chiral antiferromagnet. *Nature Physics*, 13(11):1085–1090, 2017.

[21] C. Wuttke, F. Caglieris, S. Sykora, F. Scaravaggi, A. U. B. Wolter, K. Manna, V. Süss, C. Shekhar, C. Felser, B. Büchner, et al. Berry curvature unravelled by the anomalous nernst effect in Mn_3Ge. *Physical Review B*, 100(8):085111, 2019.

[22] Mn_5Si_3 crystal structure: Datasheet. `https://materials.springer.com/isp/crystallographic/docs/sd_0526576`. Part of SpringerMaterials.

[23] M. Gottschilch, O. Gourdon, J. Persson, C. de la Cruz, V. Petříček, and T. Brueckel. Study of the antiferromagnetism of Mn_5Si_3: an inverse magnetocaloric effect material. *Journal of materials chemistry*, 22(30):15275–15284, 2012.

[24] H. Reichlová, T. Janda, J. Godinho, A. Markou, D. Kriegner, R. Schlitz, J. Železný, Z. Šobáň, M. Bejarano, H. Schultheiss, et al. Imaging and writing magnetic domains in the non-collinear antiferromagnet Mn_3Sn. *Nature communications*, 10(1):1–6, 2019.

[25] A. Husmann and L. J. Singh. Temperature dependence of the anomalous hall conductivity in the heusler alloy Co_2CrAl. *Physical Review B*, 73(17):172417, 2006.

[26] R Schlitz, P. Swekis, A. Markou, H. Reichlová, M. Lammel, J. Gayles, A. Thomas, K. Nielsch, C. Felser, and S. T. B. Goennenwein. All electrical access to topological transport features in $Mn_{1.8}PtSn$ films. *Nano letters*, 19(4):2366–2370, 2019.

[27] F. Hecht. New development in FreeFem++. *Journal of numerical mathematics*, 20(3-4):251–266, 2012.

[28] T. Ostatnický. Private communication, 2019-12-04.

[29] Mn_3Sn crystal structure: Datasheet. `https://materials.springer.com/isp/crystallographic/docs/sd_0453998`. Part of SpringerMaterials.

[30] M. Lax. Temperature rise induced by a laser beam. *Journal of Applied Physics*, 48(9):3919–3924, 1977.

[31] W. C. Dash and R. Newman. Intrinsic optical absorption in single-crystal germanium and silicon at 77 K and 300 K. *Physical review*, 99(4):1151, 1955.

[32] P. Virtanen, R. Gommers, T. E. Oliphant, M. Haberland, et al. SciPy 1.0: Fundamental Algorithms for Scientific Computing in Python. *Nature Methods*, 17:261–272, 2020.

[33] C. J. Glassbrenner and G. A. Slack. Thermal conductivity of silicon and germanium from 3 K to the melting point. *Phys. Rev.*, 134:A1058–A1069, May 1964.

[34] H. R. Philipp and E. A. Taft. Optical constants of silicon in the region 1 to 10 eV. *Physical Review*, 120(1):37, 1960.

[35] B. J. Frey, D. B. Leviton, and T. J. Madison. Temperature-dependent refractive index of silicon and germanium. In *Optomechanical technologies for Astronomy*, volume 6273, page 62732J. International Society for Optics and Photonics, 2006.

[36] W. Fulkerson, J. P. Moore, R. K. Williams, R. S. Graves, and D. L. McElroy. Thermal conductivity, electrical resistivity, and seebeck coefficient of silicon from 100 to 1300 K. *Physical Review*, 167(3):765, 1968.

[37] L. Nadvorník. *Relativistic spintronic effects in semiconductor structures.* PhD thesis, Charles University, Prague, 2016.

List of Figures

1.1 Examples of collinear and noncollinear antiferromagnets 7
1.2 The susceptibility of an AFM as a function of temperature 8
1.3 Schematic illustrations of magnetotransport phenomena 10
1.4 Schematic illustrations of thermotransport phenomena 11

2.1 Magnetic structure of Mn_5Si_3 14
2.2 Temperature dependence of magnetization measured by SQUID magnetometry 15
2.3 Schematics of devices used for measurements 16
2.4 Devices for magnetotransport measurement and their electrical connection 17
2.5 Devices for thermotransport measurements and their electrical connection 18
2.6 Thermal gradient reversal technique 19
2.7 Calibration of thermometers on Nernst devices 19
2.8 Behaviour of temperature difference measured by the thermometers 20
2.9 On the principle of scanning thermal gradient microscopy 22
2.10 Experimental setup of a experiment using scanning thermal gradient microscopy 22
2.11 Vector quantities during scanning thermal gradient microscopy with laser beam near to the sample border 23

3.1 Temperature dependence of sample resistivity 25
3.2 On the analysis of transverse resistance data 27
3.3 Behaviour of transverse resistance during z-field sweeps in Hall geometry for different temperatures, samples 52, 58 and 80 29
3.4 Behaviour of transverse resistance during z-field sweeps in Hall geometry for different temperatures, sample 82 30
3.5 Behaviour of longitudinal resistance during z-field sweeps in Hall geometry for different temperatures 32
3.6 Temperature dependence of effective coercive field H_c^{eff}, transverse conductivity σ_{xy}, and magnetoresistace at MR in Hall geometry . 33
3.7 Behaviour of transverse conductivity during magnetic field (2 T) rotations at 10 K in Hall geometry 35
3.8 Transverse signal during z-field sweeps in Nernst geometry for 40 and 60 K 36
3.9 Longitudinal signal during z-field sweeps in Nernst geometry for 40 and 60 K 37
3.10 Maps of longitudinal and transverse voltages at 90 K created using scanning thermal gradient microscopy 39

3.11 Map of $V_{xx}^{(y)}$ voltage at room temperature for both polarities of field using 725-nm and 900-nm laser 40
3.12 Map of $V_{xx}^{(y)}$ voltage at 40 K, 90 K, and RT for both polarities of field 41

4.1 Modelling of an ANE response in an STGM experiment 43
4.2 Computed map of transverse voltage generated by the anomalous Nernst effect 46
4.3 Optimization of the device shape 46
4.4 Rounding the edges of the transverse contact connection as a method for optimizing the devices 47
4.5 Schematics of modelling Seebeck response from silicon substrate in a scanning thermal gradient microscopy experiment 48
4.6 Computed dependence of longitudinal voltage induced by the Seebeck effect in silicon on the position of the laser beam 50

A.1 Measurement of laser spot width 59

List of Tables

1.1 Classes of materials based on their susceptibility 6

2.1 Overview of the samples and their properties 14
2.2 Magnitude of thermal gradient 21

List of Abbreviations

AFM	antiferromagnet,
AHE	anomalous Hall effect,
AMR	anisotropic magnetoresistance,
ANE	anomalous Nernst effect,
cAFM	collinear antiferromagnetic (ordering, phase),
CINaM	Centre Interdisciplinaire de Nanoscience de Marseille,
FEM	finite element method,
FWHM	full width at half maximum,
MR	magnetoresistance,
nAFM	noncollinear antiferromagnetic (ordering, phase),
OHE	ordinary Hall effect,
ONE	ordinary Nernst effect,
PNE	planar Nernst effect,
ScEM	scanning edge method,
SPINTEC	Spintronique et technologie des Composants,
SQUID	superconducting quantum interference device,
STGM	scanning thermal gradient microscopy,
tAMR	thermal anisotropic magnetoresistance,
THE	topological Hall effect.

Appendix A

Determination of laser spot width

The laser spot width was determined using the scanning edge method (ScEM) in reflective geometry. We suppose that the transversal profile of the beam is Gaussian and is thus described by the following equations for electric field and intensity [37]:

$$E = E_0 \exp\left(-\frac{r^2}{w^2}\right), \quad I = |E|^2 = I_0 \exp\left(-\frac{2r^2}{w^2}\right), \tag{A.1}$$

where r is the radial coordinate, E_0 and I_0 amplitudes and w is a parameter of the Gaussians. The technique employs scanning with laser spot over an edge between materials of different reflectance (see Fig. A.1 (a)): as the beam moves

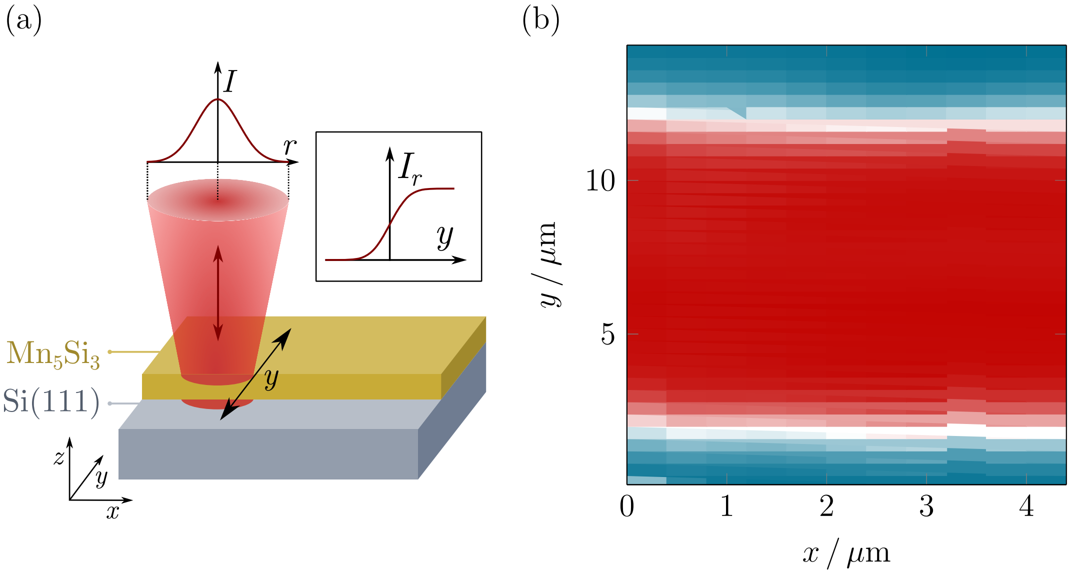

Figure A.1: Measurement of laser spot width. (a) Schematic depiction of the scanning edge method: the Gaussian beam moves across the edge of the sample, which generates dependence of reflected intensity I_r on y as shown. (b) Map of reflectance at zero field and room temperature: the map displays dependence of intensity measured by the Si detector on the beam position (in arb. u.: red corresponds to high signal, blue to low).

in a perpendicular direction to the edge, the intensity of the reflected beam varies in the following manner:

$$I_r(y) = \int_{-\infty}^{\infty}\int_{-\infty}^{y} \exp\left(-2\frac{x'^2+y'^2}{w^2}\right)\mathrm{d}x'\mathrm{d}y' = \frac{\pi w^2}{4}\left[1+\mathrm{erf}\left(\frac{\sqrt{2}y}{w}\right)\right], \qquad \text{(A.2)}$$

where y is the axis perpendicular to the edge and $\mathrm{erf}\,(\xi) = \int_0^{\xi}\exp\left(-t^2\right)\mathrm{d}t$ is the error function [37]. If we fit experimentally measured data by Eq. A.2, we get w, which is related to the full width at half maximum of the I distribution FWHM as follows:

$$\mathrm{FWHM} = \sqrt{2\ln 2}\, w. \qquad \text{(A.3)}$$

As we have had to focus the beam for every change in temperature or magnetic field and the focusing was done in a heuristic way by observing the laser spot on the CCD camera, the spot size has varied for every adjustment of external conditions. Together with recording transversal and longitudinal voltages during a STGM scan, we have also measured reflected intensity I_r. An example of such a reflectance map is shown in Fig. A.1 (b): the red area (high values of I_r) represents the sample, while blue color indicates substrate. These maps were then employed to determine the spot sizes: since the maps were also obtained by scanning with the laser beam over the sample, we have simply used one edge of the sample to compute FWHM using ScEM (this was done every time when the beam crossed the edge) and have averaged all these values over one reflectance map. The resulting FWHM fluctuated between 1.6 μm and 2.7 μm.